

# Broadband Kinetic-Inductance Parametric Amplifiers with Impedance Engineering

Chih-Chiao Hung,<sup>1,\*</sup> Hiroki Kutsuma,<sup>2</sup> Chung Wai Sandbo Chang,<sup>1</sup>

Arjan Ferdinand van Loo,<sup>1,3</sup> and Yasunobu Nakamura<sup>1,3,†</sup>

<sup>1</sup>*RIKEN Center for Quantum Computing (RQC), Wako, Saitama 351-0198, Japan*

<sup>2</sup>*Graduate School of Engineering, Tohoku University, Sendai 980-8579, Japan*

<sup>3</sup>*Department of Applied Physics, Graduate School of Engineering,*

*The University of Tokyo, Bunkyo-ku, Tokyo 113-8656, Japan*

(Dated: April 25, 2025)

Broadband quantum-limited parametric amplifiers (PAs) are essential components in quantum information science and technology. Impedance-engineered resonator-based PAs and traveling-wave PAs are the primary approaches to overcome the gain–bandwidth constraint. While the former PAs are simpler to fabricate, the target characteristic impedance  $Z_{\text{NR}}$  of the nonlinear resonator has been restricted to be below  $10\ \Omega$ , requiring large capacitance. Moreover, these PAs have only been implemented with aluminum-based Josephson junctions (JJs), hindering their operation at high temperatures or strong magnetic fields. To address these issues, we propose a three-stage impedance-transformer scheme, showcased with a 20-nm-thick, 250-nm-wide high-kinetic-inductance niobium-titanium-nitride (NbTiN) film. Our scheme enables  $Z_{\text{NR}}$  up to several tens of ohms—a tenfold improvement over conventional designs, achieved through an additional quarter-wavelength transmission line with the characteristic impedance of  $180\ \Omega$ . Our kinetic-inductance impedance-engineered parametric amplifiers (KIMPA), featuring a 330-fF shunt capacitor, demonstrate a phase-preserving amplification with a 450-MHz bandwidth at 17-dB gain, and an added noise ranging from 0.5–1.3 quanta near the center frequency of 8.4 GHz. Due to the high critical current of the NbTiN nanowire, the KIMPA also achieves a saturation power of up to  $-68\pm 3$  dBm, approximately 30-dB higher than that of JJ-based PAs. This scheme also opens new possibilities for other three-wave-mixing building blocks.

## I. INTRODUCTION

Quantum-noise-limited microwave parametric amplifiers (PAs), which exploit parametric photon conversion, have become indispensable for sensitive quantum device readouts in multiple scientific fields [1–4]. Their effectiveness stems from the strategic placement at the first-signal-amplification stage, typically located at the lowest temperature, while providing sufficient gain to overcome noise from subsequent stages including high-electron-mobility-transistor (HEMT) amplifiers. These PAs have significantly enhanced qubit-state discrimination in superconducting quantum information research [3, 5] and enabled the detection of previously indiscernible weak signals in high-sensitivity spin resonance experiments [6–8] and dark matter searches of axions [9–11]. With the progression of quantum computing toward fault-tolerant systems that necessitate concurrent multi-qubit readout [5] and error correction [12, 13], there is an increasing demand for next-generation PAs with attributes of low added noise, wide bandwidth, and high saturation power.

Al-AIO<sub>x</sub>-Al Josephson junctions (JJs) have long served as amplifying elements [14], offering controllable nonlinearity through oxidation conditions. Although JJ-based PAs demonstrate near-ideal quantum efficiency [15–17], they are limited to operation below the critical temperature  $T_c$  of aluminum and in low magnetic fields. More-

over, their saturation power (or 1-dB compression power)  $P_{1\text{dB}}$  ranges from  $-100$  to  $-93$  dBm [3, 18, 19] due to relatively low critical currents and higher-order nonlinearities [20], presenting challenges for simultaneous readouts of tens of qubits [21].

In contrast, kinetic-inductance (KI) materials such as NbN and NbTiN offer distinct advantages: high operating temperature [22–24] due to high  $T_c$  [25] and high  $P_{1\text{dB}}$  ( $-65$  to  $-55$  dBm) [22, 26–28] attributed to larger critical currents compared to JJs [29]. Additionally, their larger superconducting gaps [24, 30, 31] enable better performance in strong magnetic fields [8, 32] and potentially higher operating temperatures and frequencies. Generally, the lower intrinsic nonlinearity of KI materials [28] necessitates higher pump powers to achieve comparable bandwidth and gain to JJ-based designs. As such, JJ-based PAs might be better for some applications, while the choice between JJ- and KI-based PAs involves operating conditions, required dynamic ranges, and pump-power constraints, making these trade-offs crucial for amplifier design.

The pioneering PA generations exhibited a fixed gain–bandwidth product [15, 16], where increased gain came at the cost of reduced operational frequency range (bandwidth). Recent efforts to overcome this limitation have followed two main approaches. Traveling-wave parametric amplifiers (TWPAs), utilizing thousands of nonlinear unit cells as transmission lines, have achieved bandwidths approaching 4 GHz [3, 26]. However, they suffer from gain ripples due to the impedance mismatches [26, 33] and exhibit relatively low quantum effi-

\* chih-chiao.hung@riken.jp

† yasunobu@ap.t.u-tokyo.ac.jp

ciency compared to conventional PAs due to the higher dissipation of lossy dielectrics [34]. An alternative approach utilizes passive networks like Klopfenstein tapers [35] or impedance transformers [17, 18, 36–38] to reduce the external quality factor of lumped-element nonlinear oscillators, which operate in the reflection mode and require circulators. These designs, demanding minimal fabrication resources, attain flat-top gain profiles with small ripples and near-quantum-limited noise performance. However, these impedance-engineered PAs require large shunt capacitances of several picofarads and sometimes employ parallel-plate capacitors with possible additional loss from the dielectrics [17, 35, 36] (see Appendix E). Furthermore, they are limited to JJs rather than KI materials.

Here, we propose an impedance-engineering scheme using a “three-stage impedance transformer” [Fig. 1(a)] to reduce the shunt capacitance to a few-hundred femtofarads while achieving a wide bandwidth and maintaining a simple fabrication recipe. We demonstrate this approach using a NbTiN thin film and discuss its nonlinear properties in Sec. III, along with fabrication details in Sec. IV. Performance of the KI-based impedance-engineered PA (KIMPA) is presented in Sec. V: 17-dB signal gain, 450-MHz bandwidth,  $-68 \pm 3$ -dBm saturation power, and 0.5–1.3-quanta added noise.

## II. THREE-STAGE IMPEDANCE TRANSFORMER

The nonlinearity of PAs under pumped conditions can be modeled by treating the impedance of the nonlinear element (typically an inductor) as a purely imaginary component in parallel with an effective negative resistance [38, 39], resulting in gain [40]. The time-dependent inductance modulated at the pump frequency  $\omega_p$  follows

$$L(t) = L_0 + \frac{1}{2} (\delta L e^{i\omega_p t} + \text{c.c.}), \quad (1)$$

where  $L_0$  is the unmodulated inductance, and  $\delta L$  denotes the complex modulation amplitude. A nonlinear resonator (NR) consisting of a time-dependent  $L(t)$  in parallel with a capacitor enables three-wave-mixing (3WM) parametric amplification by converting a pump photon at  $\omega_p$  into a signal photon at  $\omega_s$  and an idler photon at  $\omega_i$ , when  $\omega_p = \omega_s + \omega_i$ . For the examination of non-degenerate amplification ( $\omega_s \neq \omega_i$ ), we aim to replace the time-dependent  $L(t)$  with an effective time-independent inductor  $L_{\text{eff}}$ .

To determine  $L_{\text{eff}}$ ,  $L(t)$  is initially analyzed as the central set of three elements that link the signal- and idler-port currents through the signal (in blue) and idler (in lavender) matching networks as illustrated in Fig. 1(b) [38]. These three elements consist of one amplification inverter ABCD matrix ( $\mathbf{J}_{\text{PA}}$ ), which characterizes the parametric coupling of signal and idler currents, and two parallel time-independent  $L'_0$  compo-

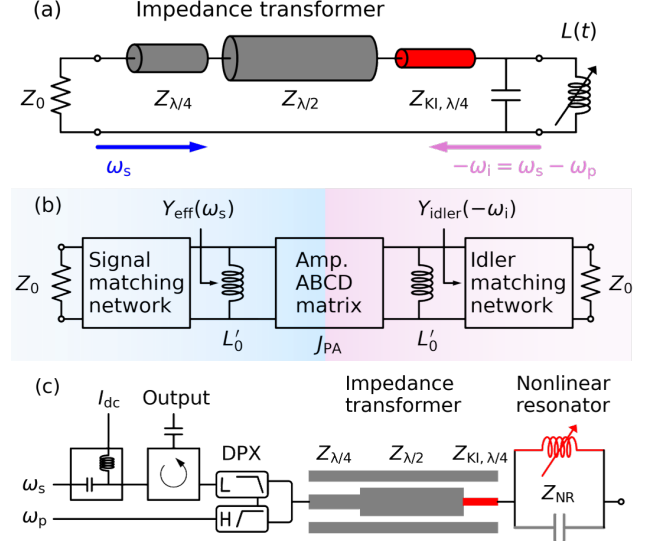


FIG. 1. (a) Circuit diagram of our kinetic impedance-engineered parametric amplifier (KIMPA). The three-stage impedance transformer, consisting of two quarter-wavelength ( $\lambda/4$ ) and one half-wavelength ( $\lambda/2$ ) transmission lines, broadens the bandwidth of the nonlinear resonator (NR) consisting of a shunt capacitor and a modulated inductor  $L(t)$ . The resonance of NR is close to the resonance of the  $\lambda/2$  line. (b) Equivalent time-independent circuit diagram. The amplification ABCD matrix describes the relationship of signal and idler currents, sent from the left and the right, respectively. The signal (blue) and the idler (lavender) segments undergo frequencies of  $\omega_s$  and  $-\omega_i$ , respectively. (c) Schematic diagram of (a) on the right and the experimental setup on the left. The signal path incorporates a bias tee for the dc current ( $I_{\text{dc}}$ ) injection and a diplexer for combining the signal and pump. The device is fabricated using two materials, NbTiN (red) and aluminum (gray). The nonlinear resonator has a characteristic impedance  $Z_{\text{NR}}$ .

nents (for derivation details, refer to Appendix A 1). Here,  $L'_0 = L_0(1 - \alpha)$  depends on the dimensionless modulation strength  $\alpha = |\delta L|^2 / 4L_0^2$ . Note that the idler component (right side of  $\mathbf{J}_{\text{PA}}$  in lavender) arises from the idler current at  $-\omega_i$ , distinct from the signal counterpart experiencing  $\omega_s$ . Moreover, the idler matching network mirrors the signal circuit, incorporating components between the port and  $L(t)$  within two pairs of open dots in Fig. 1(a). The series of matching networks of the signal and the idler is highlighted by blue and lavender arrows in Fig. 1(a).

In Appendix A 1, we summarize the complicated circuit described above into an effective time-independent admittance  $Y_{\text{eff}}$  to represent  $L(t)$  as:

$$Y_{\text{eff}}(\omega_s) = \frac{1}{i\omega_s L'_0} \left[ 1 + \frac{\alpha}{i\omega_i L'_0 Y_{\text{idler}}^*(\omega_i) - 1} \right] \quad (2)$$

$$= \frac{1}{i\omega_s L_{\text{eff}}}, \quad (3)$$

where  $Y_k$  ( $k = \text{idler}, \text{eff}$ ) are defined as the admittance looking from the arrow direction in Fig. 1(b).  $L_{\text{eff}}$  is a complex number that can resemble a standard inductor parallel to a resistor with a negative value under a suitable impedance-matching network (related to  $Y_{\text{idler}}$ ) and a proper pump current (see Appendix A 2). Since  $Y_{\text{idler}}$  is the admittance looking from the inductor to the idler port,  $Y_{\text{idler}}(-\omega_i) = Y_{\text{idler}}^*(\omega_i)$ .

The bandwidth  $\Delta\omega$  of PAs for any negative-resistance devices can be designed and calculated [40]. In a basic signal-matching network with an NR linking to a port via a coupled capacitor, the PA faces the gain–bandwidth product limitation, qualifying it as a single-pole PA [38]. Conversely, for more intricate networks involving coupling to multiple resonances with  $N \geq 1$  modes—such as lumped-element resonators [19] or half-wavelength  $\lambda/2$  coplanar waveguides (CPWs) [17]—the PA evolves into a  $(N+1)$ -pole system, featuring  $N+1$  local gain maxima, surpassing the gain–bandwidth product limitation.

By selecting the desired bandwidth, signal gain, and a filter type (e.g., Chebyshev, Butterworth, etc.), one can map a multiple-pole PA, which is often called an impedance-engineered PA (IMPA), into a band-pass impedance-matching network [38, 40]. We introduce a novel three-stage impedance-transformer matching network as an example of a two-pole system, depicted in Fig. 1(a). This two-pole PA features a  $\lambda/2$  CPW resonator, an NR, and two  $\lambda/4$  CPWs acting as an impedance inverter. Unlike the conventional setup in Ref. 17, which lacks the red  $\lambda/4$  CPW in Fig. 1(a), our design supports a broader range for the characteristic impedance  $Z_{\text{NR}}$  of a NR, necessitating a shunt capacitance of a few-hundred femtofarads rather than several picofarads. The key improvement of our scheme is this additional  $\lambda/4$  CPW with a high impedance of  $Z_{\text{KI},\lambda/4} = 180 \Omega$ , placed between the  $\lambda/2$  CPW resonator and the NR. Achieving such a high-impedance CPW involves specialized methods, like using the kinetic inductance of NbTiN, since  $Z_{\text{KI},\lambda/4}$  exceeds the standard CPW geometric-impedance limit of about  $90 \Omega$  (for a  $1\text{-}\mu\text{m}$ -wide center line and  $20\text{-}\mu\text{m}$  gap). In our design, we set  $Z_{\text{NR}} = 60 \Omega$  (corresponding to a  $330\text{-fF}$  shunt capacitance at  $8 \text{ GHz}$ ),  $Z_{\lambda/4} = 80 \Omega$ , and  $Z_{\lambda/2} = 30 \Omega$ . A detailed designing procedure is provided in Appendix A 2.

### III. KINETIC-INDUCTANCE PROPERTIES

The nonlinearity of kinetic-inductance materials arises from the inertia of Cooper pairs resisting changes in their velocity and becomes more pronounced in thinner films and under current bias. For films much thinner than their penetration depth, the kinetic inductance is given by

$$L_{\text{k}0} = \frac{\hbar}{\pi\Delta_0} \frac{\rho_n}{d} \frac{l}{w}, \quad (4)$$

where  $\Delta_0$  is the superconducting gap energy,  $\rho_n$  is the normal-state resistivity,  $l$ ,  $w$ , and  $d$  are the KI material's length, width, and thickness, respectively [25]. An injected current enhances  $L_{\text{k}0}$ , and we may write an expansion of the current-dependent kinetic inductance [25]

$$L_{\text{k}}(I) = L_{\text{k}0} \left( 1 + \frac{I^2}{I_*^2} + \dots \right), \quad (5)$$

where  $I_*$  is the current scale determining the sensitivity (see Appendix C for a detailed discussion). This is typically approximated as a parabolic function when  $I_* \gg I$  and written as

$$L_{\text{k}}(I) \approx L_{\text{k}0} \left( 1 + \frac{I^2}{I_*^2} \right). \quad (6)$$

Considering a modulated current with a constant offset,  $I = I_{\text{dc}} + I_{\text{ac}}$ , the kinetic inductance becomes

$$L_{\text{k}} \approx L_{\text{k}0} \left( 1 + \frac{I_{\text{dc}}^2}{I_*^2} + \frac{2I_{\text{dc}}I_{\text{ac}}}{I_*^2} + \frac{I_{\text{ac}}^2}{I_*^2} \right). \quad (7)$$

The fourth term is associated with the Kerr coefficient allowing the four-wave-mixing (4WM) process, where two pump photons are transformed into signal and idler photons, necessitating  $2\omega_p = \omega_s + \omega_i$ , and becomes negligible when  $I_* \gg |I_{\text{ac}}|$  as in the case of the NbTiN nanowire we use (see Appendix B). In Appendix C, we divide  $I_{\text{ac}}$  into a dominant pump current  $I_p$  and a weak signal current represented by a quantum operator, resulting in  $\alpha \propto |I_p|^2$ .

Although some KI-based PAs employ the 4WM process [26, 33], the three-wave-mixing process offers advantages in  $P_{1\text{dB}}$  [41, 42] and enables simple pump removal through passive elements (e.g. diplexers) due to a large frequency separation from the signal. In Fig. 1(c), a simplified wiring diagram illustrates the paths for the dc current, the signal, and the pump. A bias tee combines the dc current and the signal frequency before entering the circulator, which redirects the reflected signal into the readout amplification chain. The diplexer combines the pump and the signal into the three-stage impedance transformer.

### IV. FABRICATION PROCESS

Our devices incorporate two superconducting materials: high-kinetic-inductance NbTiN and aluminum. In Fig. 1(c), we emphasize two different materials with colors, red for NbTiN and gray for aluminum, in the circuit scheme. In Figs. 2(a) and (b), the NbTiN exposed to air is marked in red, while the remaining electrodes are aluminum-coated on top of NbTiN. In Appendix B, we demonstrate that resonators with resonances around  $8.5 \text{ GHz}$  and nanowire inductors consisting of a thin NbTiN film, constructed through the fabrication methods detailed below, exhibit internal quality factors  $Q_i \approx 10^5$ .

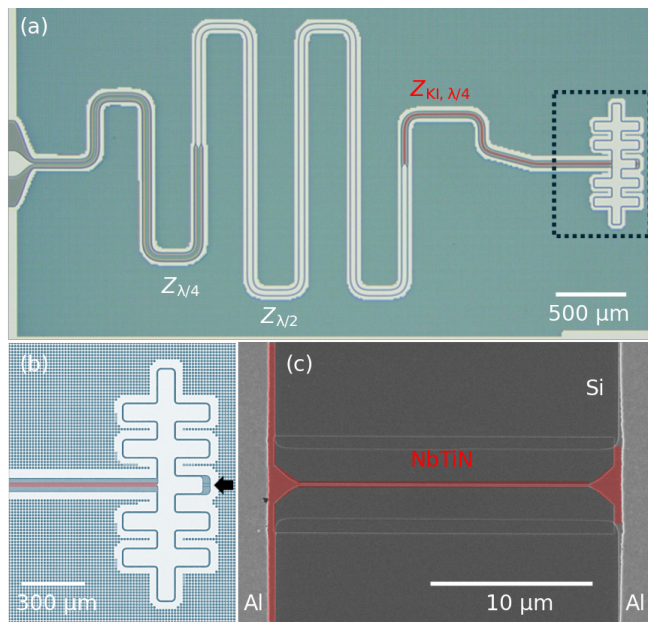


FIG. 2. (a) Optical images of the device. (b) Magnified image of the dotted rectangular zone in (a). The high-impedance  $\lambda/4$  CPW has a center conductor ( $2 \mu\text{m}$  in width) made of NbTiN (red). All other electrodes and ground planes are covered with 120-nm-thick aluminum with low KI. There are high-density holes in the ground plane to trap stray vortices. The black arrow points at the location of the NbTiN nanowire. (c) Scanning-electron-microscope image showing a 250-nm-wide NbTiN nanowire inductor (red).

Fabrication begins with cleaning a 3-inch 300- $\mu\text{m}$ -thick high-resistivity silicon wafer using hydrofluoric acid (HF) to remove surface oxide, followed by sputtering of NbTiN at room temperature. We then pattern nanowire inductors using electron-beam lithography with ZEP520A resist and etch the exposed and developed regions using  $\text{CF}_4$  dry etching. Subsequently, we define the CPWs, PAs, and vortex traps through photolithography using AZ1500-4.4cp resist and  $\text{CF}_4$  dry etching. After another HF cleaning step, we perform ion-milling surface cleaning under a vacuum before depositing aluminum of 150 nm. The aluminum layer is then patterned with photolithography and wet etched to cover all electrodes except high-impedance  $\lambda/4$  CPWs and nanowire inductors. This Al-on-NbTiN bilayer serves a few purposes: (i) ensuring low kinetic inductance to match our COMSOL simulations, (ii) reducing the radiation loss, and (iii) reducing stray inductance. Without aluminum, two CPW sections would require CPW center widths  $w$  several times larger than our current design, leading to extra radiation loss  $1/Q_{\text{rad}} \propto w^2$  [25, 43]. Furthermore, increased stray inductance would dilute the nonlinearity and effectively enhance  $I_*$ , requiring more pump power. Finally, the wafer is coated with a protective photoresist layer, diced into  $2.5 \times 5 \text{ mm}^2$  chips, and cleaned with N-Methylpyrrolidone remover.

## V. DEVICE PERFORMANCE

### A. Gain measurement

The devices are measured in a dilution refrigerator at a base temperature of 10 mK. The amplitude and phase of the reflection coefficient  $S_{11}$  are shown in Figs. 3(a) and (b). The NR resonance frequency in the absence of  $I_{\text{dc}}$  is approximately 9.6 GHz. The measurement curve in blue exhibits noticeable ripples arising from impedance mismatches at the wire bonding, circulators, diplexers, etc. The distance between impedance mismatches creates standing waves that affect the gain profile through constructive or destructive interference depending on the frequency. The experimental setup significantly influences the gain profile even for identical devices, which is a phenomenon noted in previous studies [17, 35, 37]. To minimize interference effects, we directly connect the diplexer and circulator, eliminating interconnecting cables.

The non-ideal environment is modeled as two superimposed sinusoidal waves on top of the 50- $\Omega$  baseline:

$$Z_{\text{env}}(\omega) = Z_0 + Z_1 e^{i(\omega\tau_1 + \phi_1)} + Z_2 e^{i(\omega\tau_2 + \phi_2)}, \quad (8)$$

where  $Z_0 = 50 \Omega$ ,  $Z_n$  ( $n=1,2$ ) is the amplitude of periodic modulations,  $\tau_n$  is the period, and  $\phi_n$  is the phase offset. The orange curve shows our numerical calculation with parameters  $Z_1 = 14.2 \Omega$ ,  $Z_2 = 1.9 \Omega$ ,  $\tau_1/2\pi = 10.5 \text{ ns}$ ,  $\phi_1 = -0.7\pi$ , and  $\tau_2/2\pi = 121 \text{ ns}$ , and  $\phi_2 = 0$  to match the ripple of a period of  $\sim 450 \text{ MHz}$  and a 4-dB amplitude. Interestingly,  $\tau_1$  corresponds to approximately a 17-cm coaxial cable with a phase velocity of  $2 \times 10^8 \text{ m/s}$ , closely matching the device-to-circulator distance.

To characterize the amplifier's performance, we apply  $I_{\text{dc}}$  ranging from 530 to 600  $\mu\text{A}$  to tune the NR close to 8.47 GHz. The pump frequency  $\omega_p$  is set to approximately twice the resonance frequency, with the pump power  $P_p$  gradually increasing until reaching the superconductivity-breaking point  $P_p^{\text{SC}}$ . An example of the measured signal gain  $G_s$  vs  $\Delta\omega_s = \omega_s - \omega_p/2$  at different  $P_p$  is shown in Figs. 3(c) and (d). The amplifier exhibits a 450-MHz bandwidth with a signal gain exceeding 17 dB. We observe that the curve at  $P_p = -29.6 \text{ dBm}$  has ripples in the valley between two peaks due to the impedance mismatch, which become more pronounced at higher pump powers and higher gain. A center peak grows with  $P_p$ , and eventually  $G_s$  exceeds 40 dB, but this comes at the cost of the reduced gain-bandwidth product, whose behavior is captured also in the simulation as described in Appendix D. When  $P_p > P_p^{\text{SC}} = -28.4 \text{ dBm}$ , the superconductivity breaks down, resulting in complete loss of amplification. Recovering the superconducting state requires turning off both the pump and dc current.

Figure 3(e) reveals a maximum bandwidth of 470 MHz. However, as  $P_p$  approaches  $P_p^{\text{SC}}$ , there is an increase in the stochastic superconductivity breaking events, likely

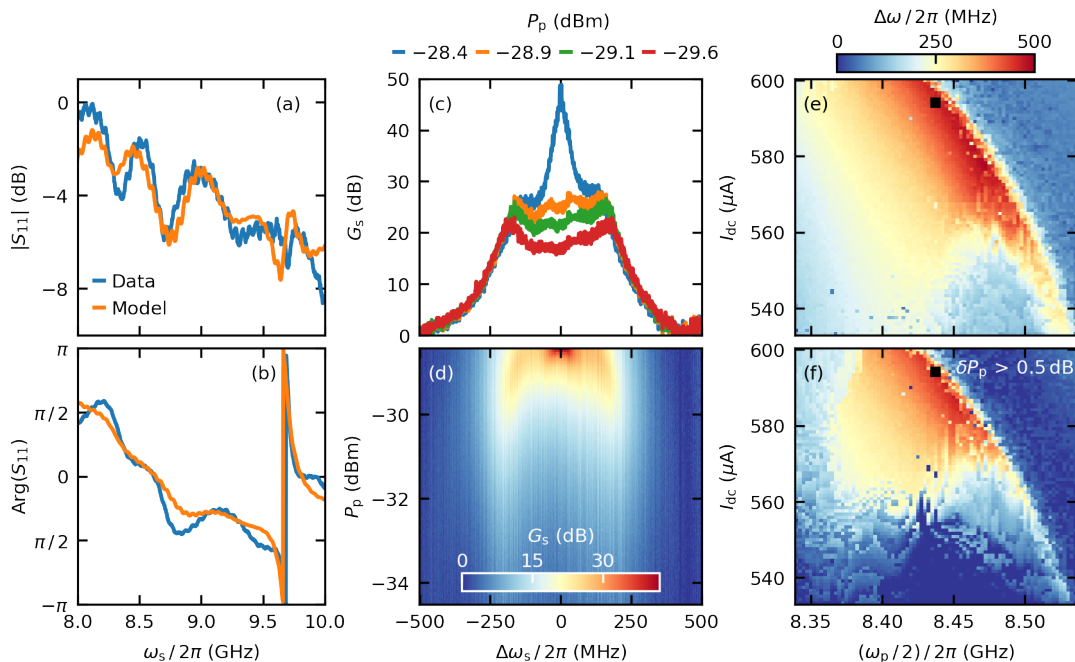


FIG. 3. Characterization of the kinetic-inductance impedance-engineered parametric amplifier (KIMPA). (a) Amplitude and (b) phase of the reflection coefficient  $S_{11}$  vs signal frequency  $\omega_s$  (blue) and the numerical simulation (orange). (c) Signal gain  $G_s$  vs signal frequency  $\omega_s$  detuned from half the pump frequency  $\omega_p$  by  $\Delta\omega_s = \omega_s - \omega_p/2$ , at different pump powers  $P_p$ . (d)  $G_s$  as a function of  $\Delta\omega_s$  and  $P_p$ . (e) Bandwidth  $\Delta\omega$  at 17-dB gain as a function of  $\omega_p$  and  $I_{dc}$ . (f) Refined bandwidth map subject to a stability criterion  $\delta P_p = P_p^{SC}/P_p > 0.5$  dB to ensure reliable operation. Here,  $P_p^{SC}$  is the maximum pump power before superconductivity breakdowns occur. The breakdown event rate increases further when  $P_p$  approaches  $P_p^{SC}$ . The black squares in (e) and (f) mark the operating point used in (c) and (d), chosen for the optimal balance between bandwidth and gain ripples.

because  $I_{dc} + I_{ac} \rightarrow I_c$  and a higher probability of pair-breaking photon absorption [44]. Since there is no obvious difference in the event rate of superconductivity breakdown (occurring every 2–6 hours) when  $\delta P_p = P_p^{SC}/P_p > 0.5$  dB, we set the threshold to ensure reliable operation. The revised plot is in Fig. 3(f). The black square indicates the operating parameters in Figs. 3(c) and (d), which lead to less ripple amplitude even though the bandwidth is smaller than the maximum achievable bandwidth. Interestingly, the impedance mismatch in our setup creates constructive interference that broadens the bandwidth compared to the simulation. This is discussed in detail in Appendix A 2.

### B. Saturation-power characteristics

The saturation power, characterized by the 1-dB compression point,  $P_{1dB}$ , is defined as the signal power  $P_s$  at which  $G_s$  decreases by 1 dB compared to its weak-power limit. In Fig. 4(a), we characterize  $P_{1dB}$  by incrementing  $P_s$  using the same parameters as used at the black square in Fig. 3(e) with  $P_p = -29.7$  dBm. The color map in Fig. 4(a) illustrates  $G_s$  as a function of  $\Delta\omega_s$  and  $P_s$ . Rather than exhibiting gradual compression, the gain

drops off abruptly, indicating superconductivity breakdown. We denote this critical power level as  $P_s^{SC}$ .

Two examples of the cross-section,  $P_s$  vs  $G_s$ , are shown in Fig. 4(b). Red crosses indicate  $P_{1dB}$ . At some frequencies  $P_s^{SC}$  occurs before reaching the conventional 1-dB compression point, effectively making  $P_{1dB} = P_s^{SC}$  in those cases. We plot  $P_{1dB}$  vs  $\Delta\omega_s$  in Fig. 4(c) and highlight data points in red when  $P_{1dB} = P_s^{SC}$ .

In Fig. 4(d), we have both  $G_s$  and  $P_{1dB}$  in 0.5-dB increments and observe variations in  $P_{1dB}$  even at constant gain levels, which we attribute to stochastic superconductivity-breaking events and the interference with standing-wave modes in the environment. Compared to other single-pole KI PAs in Ref. 28, our  $P_{1dB}$  is approximately 5–10 dB lower and ranges between  $-72$  and  $-66$  dBm at 17-dB gain, even though we have approximately tenfold bandwidth expecting a tenfold increase in  $P_{1dB}$  [41, 42]. This reduction might be attributed to an enhanced Kerr coefficient resulting from the small cross-section nanowire or higher-order effects induced by a much higher ratio of  $|I_p|$  over the critical current  $I_c$  than others [45].

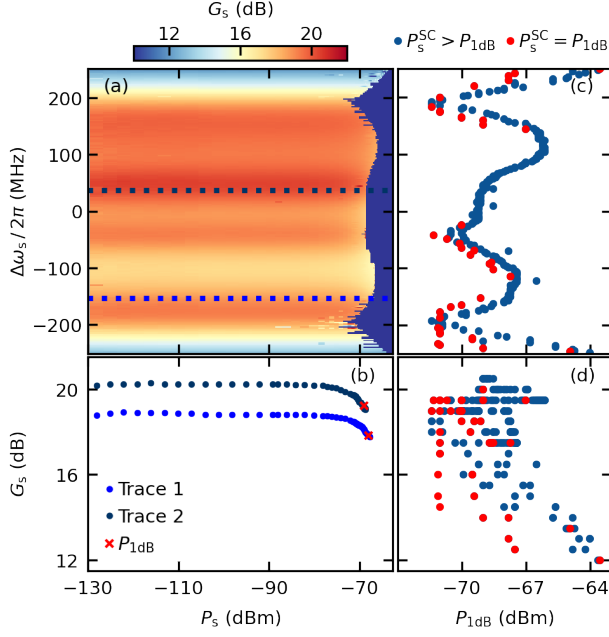


FIG. 4. Saturation-power characterization of the KIMPA. (a) Color map showing the signal gain  $G_s$  as a function of  $\Delta\omega_s$  and the signal power  $P_s$ .  $G_s$  shows an abrupt drop-off at high  $P_s$  rather than gradual compression on the right side, indicating the breakdown of superconductivity, where this power level is denoted as  $P_s^{SC}$ .  $P_s^{SC}$  is sometimes smaller than the 1-dB compression power,  $P_{1dB}$ , and thus we define  $P_{1dB} = P_s^{SC}$  in such cases. (b) Examples of gain compression curves for two different operating points, with red crosses indicating  $P_{1dB}$ . The data correspond to those on the dashed lines in (a). (c)  $P_{1dB}$  as a function of  $\Delta\omega_s$ . We mark red when  $P_{1dB} = P_s^{SC}$ . (d) Scatter plot of  $P_{1dB}$  versus the corresponding  $G_s$  in 0.5-dB increments, indicating variations in  $P_{1dB}$  even at constant gain levels.

### C. Noise characteristics

The added noise  $N_A$  of PAs determines the noise performance and is lower-bounded by the uncertainty principle of quantum mechanics to 0.5 quanta in the case of non-degenerate amplifications [46]. The circuit diagram, as depicted in Fig. 5(a), is used to model the noise added by different components. The cascaded noise equations during pumping are written as follows:

$$N_2 = G_s(N_1 + N_A), \quad (9)$$

$$N_3 = A_{23}N_2 + (1 - A_{23})N_{T_{23}}, \quad (10)$$

$$N_4 = G_{sys}(N_3 + N_{sys}). \quad (11)$$

Here,  $N_i$  ( $i = 1, 2, 3, 4$ ) is the noise at each stage,  $A_{in}$  is the loss between the input source and the PA,  $A_{23}$  is the loss between the PA and the subsequent amplifiers (HEMT plus the room temperature amplifier),  $N_{T_{23}}$  is the extra noise from the environment of the temperature  $T_{23}$ ,  $G_{sys}$  is the gain of the subsequent amplifier, and

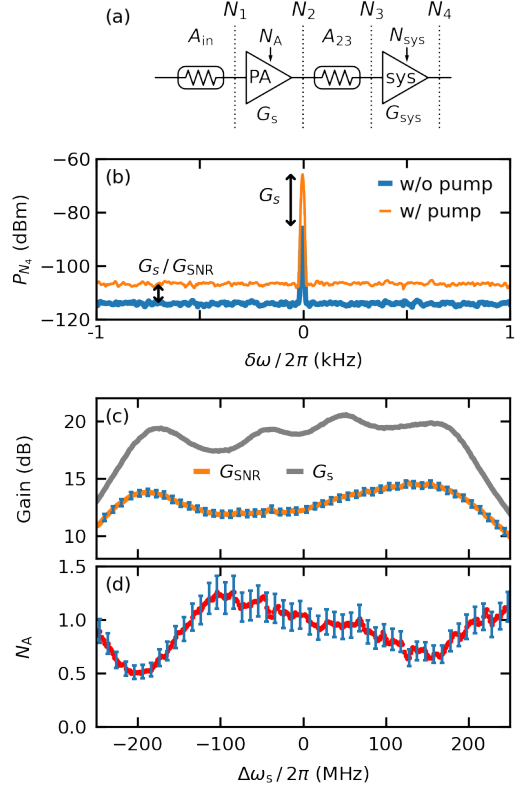


FIG. 5. (a) Model for calibrating the added noise  $N_A$ . We consider loss components,  $A_{in}$  and  $A_{23}$ , the KIMPA gain  $G_s$  and the subsequent gain  $G_{sys}$  in the measurement chain. (b) Noise spectrum obtained with a spectrum analyzer. The peak difference with and without the pump represents the KIMPA gain. Similarly, the signal-to-noise-ratio (SNR) gain  $G_{SNR}$  is indicated by the noise-floor difference as displayed in the panel. (c)  $G_{SNR}$  (orange) and  $G_s$  (gray) as a function of the signal-frequency detuning  $\Delta\omega_s$ . (d) Added noise  $N_A$  as a function of  $\Delta\omega_s$ .  $N_A$  is extracted using Eq. (12). Error bars are determined by the fitting inaccuracy and the uncertainty in the microwave component difference between the qubit and KIMPA measurement chains (see Appendix F).

$N_{sys}$  is the effective added noise. When there is enough attenuation in the input line ( $A_{in} < -80$  dB in our case) to guarantee the thermalization at  $T = 10$  mK, we can assume  $N_1 = \frac{1}{2} \coth(\hbar\omega/k_B T) \approx 0.5$  [47, 48].

In the case without pumping, we append ‘‘off’’ to  $N_i$  and assign  $N_2^{off} \approx 0.5$  because the PA is in a millikelvin environment, while the second and third equations remain unchanged. The final-stage noise  $N_4 = P_{N_4}/(\hbar\omega B_m)$  is quantified by a spectrum analyzer, where  $P_{N_4}$  is the measured background noise floor and  $B_m = 10$  Hz denotes the IF bandwidth used for the measurement. Finally, by subtracting  $N_4^{off}$  from  $N_4$ , we obtain

$$N_A = \frac{N_4 - N_4^{off}}{G_s A_{23} G_{sys}} + \frac{N_1}{G_s} - N_1. \quad (12)$$

In Fig. 5(b), we show spectra obtained from the spectrum-analyzer measurements with the pump on (orange) and off (blue), respectively. The gain in the signal-to-noise ratio  $G_{\text{SNR}}$  can be obtained by the shift of the noise floor, where  $P_{N_4}/P_{N_4}^{\text{off}} = G_s/G_{\text{SNR}}$ .  $G_{\text{SNR}}$  vs  $\Delta\omega_s$  is plotted in Fig. 5(c) compared to  $G_s$  in gray. We observe an approximate 5-dB difference between  $G_{\text{SNR}}$  and  $G_s$ .

All variables in Eq. (12) can be extracted from the spectrum analyzer, except for the effective system gain  $G_{\text{sys}}^{\text{eff}} = A_{23}G_{\text{sys}}$  calibrated using a qubit [49, 50]. We use a microwave switch to transmit the signal through a second input line, where a waveguide is coupled with a tunable transmon qubit, and measure the saturation of the transmission coefficient  $S_{21}$  of the waveguide while increasing the signal power. In Appendix F, we describe the method to obtain  $A_{\text{in}}$  and  $G_{\text{sys}}^{\text{eff}}$ .

In Fig. 5(e), the PA shows a near quantum-limited added noise with  $0.5 < N_A < 1.3$  in the bandwidth. The extra added noise  $N_{\text{ex}}$  besides the quantum-limited noise (0.5 quanta) is written as [28]

$$N_A = 0.5 + N_{\text{ex}}, \quad (13)$$

$$N_{\text{ex}} = \frac{Q_e (\sqrt{G_s} + 1)^2}{2Q_i G_s - 1} (2N_{\text{th}} + 1) + N_{\text{th}}, \quad (14)$$

$$N_{\text{th}} = \frac{1}{e^{\frac{h\nu}{k_B T}} - 1}, \quad (15)$$

where  $N_{\text{th}}$  is the thermal occupation photon number and  $Q_e$  is the external quality factor of the PA. A coaxial cable with an attenuation constant  $\alpha = 0.5$  dB/m has an internal quality factor  $Q_i = \pi/(\lambda\alpha) = 3410$  [51, 52] and the wavelength  $\lambda$  of 34 cm, while lossy elements (e.g. diplexer and microwave connectors) can further reduce  $Q_i$ . Furthermore, the strong pump raised the base temperature from 10 mK to 25 mK mainly because of the attenuation before the diplexer (see Fig. 12). Consequently, this heating induces extra thermal noise transmitted through the diplexer, augmenting the added noise of the PA unequally depending on the frequency due to impedance mismatch. More efforts are needed to minimize the standing wave effect and to verify the origins of  $N_{\text{ex}}$ .

## VI. CONCLUSION AND PROSPECTS

In this work, we have demonstrated the kinetic-inductance impedance-engineered parametric amplifier (KIMPA). Our three-stage impedance-transformer scheme successfully extended the range of impedance values for the nonlinear resonator up to several tens of ohms while reducing shunt-capacitance requirements from several picofarads to 330 fF. Using 20-nm-thick, 250-nm-wide NbTiN nanowires as the nonlinear element, the device achieved a 450-MHz bandwidth at 17-dB gain and provides approximately  $-68$ -dBm saturation power and near quantum-limited noise performance of 0.5–1.3 quanta of added noise. Our circuit shines a light

on other three-wave-mixing building blocks to implement broad-bandwidth parametric amplifiers allowing high dynamic range or operation in strong magnetic fields.

Future enhancements are possible. First of all, the impedance mismatch brings uncertainty in the bandwidth relative to the simulation, depending on the constructive or destructive interference from the coaxial-cable standing-wave modes. The on-chip diplexer integration would address two critical limitations of the existing diplexer: the substantial 10-cm footprint (compared to a half standing wavelength of 17 cm) and the problematic impedance variations that occur when transitioning from room temperature to millikelvin temperature. Secondly, improved quasiparticle protection could reduce the superconductivity-breakdown event rate. The large diplexer size hinders full  $\mu$ -metal-shield coverage for the PA, compromising protection against magnetic fields. Also, quasiparticles from the pump line persist because of insufficient attenuation, caused by the large  $|I_p|$  requirement and the insufficient pump power from the room-temperature microwave source. As demonstrated in Ref. 53, on-chip filtering can improve both pump-power efficiency and noise isolation from the pump port. Integrated on-chip diplexers and filters would consequently improve overall noise performance. Lastly, the aluminum coating on NbTiN as described in Sec. IV, while beneficial for millikelvin operation, prevents high-temperature or high-magnetic-field operation. A fully kinetic-inductance implementation of the three-stage transformer remains feasible through precise length adjustments of the CPWs to maintain quarter- and half-wavelength matching.

Interest is increasing in using alternative 3WM components for PAs, such as graphene JJs [54] and InAs nanowires [55], operating under various conditions that conventional JJs cannot. These nonlinear inductors exhibit approximately 500 pH, equivalent to  $Z_{\text{NR}} = 25 \Omega$  in an LC resonator at 8 GHz, hindering implementations in the conventional circuit. Moreover, our circuit can advantageously be applied to JJ-based PAs. Increasing the number of serial JJ units,  $M$ , could improve  $P_{1\text{dB}}$  (which scales with  $M$ ) [41] but also increases  $Z_{\text{NR}}$  (which scales with  $\sqrt{M}$ ). While JJ-based PAs with  $M = 67$  exist [18] using a conventional circuit, our circuit allows increasing  $M$  to 1000, which has shown  $P_{1\text{dB}} = -93$  dBm in a single-pole PA [56] and is expected to improve  $P_{1\text{dB}}$  by more than 10 dB using our circuit due to the external-coupling-rate improvement [41]. An additional benefit of our scheme is its pump efficiency. With the pump frequency near twice the fundamental frequency of the wavelength  $\lambda$ , the CPW lines present either half- or full-wavelength to the pump, enabling efficient transmission to the nonlinear inductance with minimal reflections.

## VII. ACKNOWLEDGMENT

We acknowledge Y. Hishida and H. Terai at the National Institute of Information and Communications

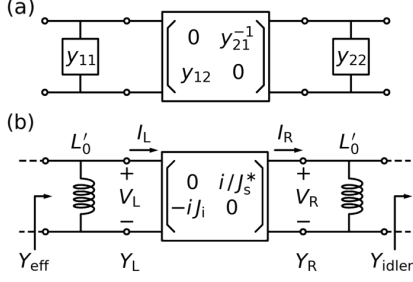


FIG. 6. Circuit diagram of a parametrically modulated inductor [Eq. (A6)]. (a) Illustration using admittance matrix parameters  $y_{ij}$  ( $i, j \in \{1, 2\}$ ). (b) Illustration of the derivation of  $Y_{\text{eff}}$ . Definitions of  $Y_i$  ( $i \in \{\text{eff}, L, R, \text{idler}\}$ ) are mentioned in the appendix.

Technology for the NbTiN-film deposition. The work was supported in part by the Ministry of Education, Culture, Sports, Science and Technology (MEXT) Quantum Leap Flagship Program (QLEAP) (Grant No. JPMXS0118068682), the JSPS Grant-in-Aid for Scientific Research (KAKENHI) (Grant No. JP22H04937), and the JSPS JRP-LEAD with UKRI (Grant No. JSP-SJRP20241713).

## Appendix A: Analysis of a synthesized impedance-matched network

### 1. Parametric amplification with a modulated inductor

Here, we provide the derivation transforming a modulated inductor to an effective time-independent inductor. The voltage  $V(t)$  across the modulated inductor  $L(t)$  is given by

$$\begin{aligned} V(t) &= \frac{V_s e^{i\omega_s t} + V_i e^{i\omega_i t} + V_p e^{i\omega_p t}}{2} + \text{c.c.} \\ &= \frac{d}{dt} [L(t)I(t)] \\ &= \frac{d}{dt} \left[ \left( L_0 + \frac{\delta L e^{i\omega_p t} + \delta L^* e^{-i\omega_p t}}{2} \right) \right. \\ &\quad \left. \times \left( \frac{I_s e^{i\omega_s t} + I_i e^{i\omega_i t} + I_p e^{i\omega_p t}}{2} + \text{c.c.} \right) \right], \end{aligned} \quad (\text{A1})$$

where the current  $I(t)$  and the voltage  $V(t)$  both have three frequency components ( $\omega_s, \omega_i$  and  $\omega_p$ ) with complex amplitudes  $I_k$  and  $V_k$  ( $k \in \{s, i, p\}$ ), respectively. Note that we assume there are no other mixing products for simplicity.

Grouping terms with the same  $e^{i\omega_s t}$  and  $e^{-i\omega_i t}$  in

Eq. (A1), we obtain

$$V_s = i\omega_s L_0 I_s + i\omega_s \frac{\delta L}{2} I_i^*, \quad (\text{A2})$$

$$V_i^* = -i\omega_i \frac{\delta L^*}{2} I_s - i\omega_i L_0 I_i, \quad (\text{A3})$$

which yields the following impedance matrix in the basis of  $(V_s, V_i^*)$  and  $(I_s, I_i^*)$ :

$$\mathbf{Z} = \begin{pmatrix} z_{11} & z_{12} \\ z_{21} & z_{22} \end{pmatrix} = \begin{pmatrix} i\omega_s L_0 & i\omega_s \delta L/2 \\ -i\omega_i \delta L^*/2 & -i\omega_i L_0 \end{pmatrix}. \quad (\text{A4})$$

From the impedance matrix, we transform to an admittance matrix  $\mathbf{Y}$  and an ABCD matrix as follows:

$$\mathbf{Y} = \begin{pmatrix} z_{22}/|z| & -z_{12}/|z| \\ -z_{21}/|z| & z_{11}/|z| \end{pmatrix} = \begin{pmatrix} y_{11} & y_{12} \\ y_{21} & y_{11} \end{pmatrix}, \quad (\text{A5})$$

$$\begin{pmatrix} A & B \\ C & D \end{pmatrix} = \begin{pmatrix} 1 & 0 \\ y_{11} & 1 \end{pmatrix} \begin{pmatrix} 0 & -1/y_{21} \\ y_{12} & 0 \end{pmatrix} \begin{pmatrix} 1 & 0 \\ y_{22} & 1 \end{pmatrix}, \quad (\text{A6})$$

where

$$|z| = z_{11}z_{22} - z_{12}z_{21} = \omega_s \omega_i L_0 L'_0, \quad (\text{A7})$$

$$y_{11} = \frac{1}{i\omega_s L'_0}, \quad (\text{A8})$$

$$y_{22} = \frac{1}{-i\omega_i L'_0}, \quad (\text{A9})$$

$$y_{12} = \frac{\delta L}{L_0} \frac{1}{i\omega_s L'_0}, \quad (\text{A10})$$

$$y_{21} = \frac{\delta L^*}{L_0} \frac{1}{i\omega_i L'_0}. \quad (\text{A11})$$

The three matrices on the right-hand side of Eq. (A6) correspond to a parallel inductor  $L'_0$  at  $\omega_s$ , an amplification inverter matrix ( $\mathbf{J}_{\text{PA}}$ ) and another parallel inductor  $L'_0$  at  $-\omega_i$ , as shown in Figs. 1(b) and 6. To be consistent with Ref. 38, we rewrite  $\mathbf{J}_{\text{PA}}$  as

$$\mathbf{J}_{\text{PA}} = \begin{pmatrix} 0 & -1/y_{21} \\ y_{12} & 0 \end{pmatrix} = \begin{pmatrix} 0 & i/J_s^* \\ -i/J_i & 0 \end{pmatrix}, \quad (\text{A12})$$

where

$$J_k = \frac{\sqrt{\alpha} e^{i\varphi_p}}{\omega_k L'_0}, \quad (\text{A13})$$

and  $\varphi_p$  is the phase of  $\delta L$ .

We aim to simplify the complex circuit into a single element with admittance  $Y_{\text{eff}}$ . Initially, we compute the admittance  $Y_{\text{idler}}$  seen from  $L'_0$  to the idler matching network as defined in Figs. 1(b) and 6(b), including a capacitor,  $Z_{\text{KL}, \lambda/4}$  line,  $Z_{\lambda/2}$  line,  $Z_{\lambda/4}$  line and  $Z_0$  source, subsequently in our case. Next, we calculate the admittance on both sides of  $\mathbf{J}_{\text{PA}}$  using  $Y_k = I_k/V_k$  ( $k \in \{L, R\}$ ), where  $I_k$  and  $V_k$  are specified in Fig. 6(b). According to the ABCD matrix formalism,  $V_L = BI_R = iI_R/J_s$  and

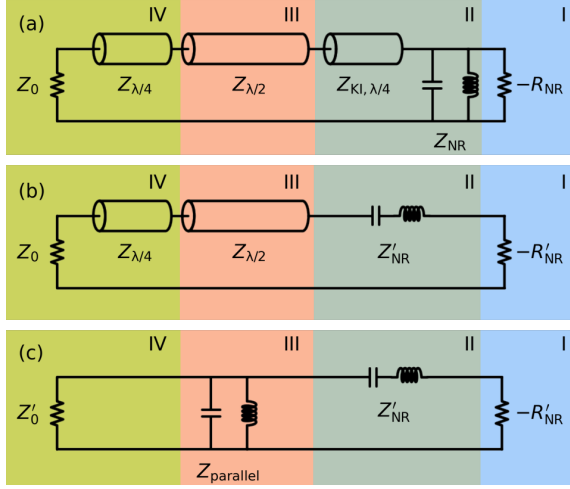


FIG. 7. Illustrations of the circuit transformation. (a) Three-stage impedance transformer. The time-dependent inductor under a frequency modulation is linearized into time-independent elements: an inductor in parallel with negative resistance  $-R_{NR}$ . (b) Intermediate step transferring the parallel RLC circuit and the  $Z_{Kl, \lambda/4}$  line into a series RLC circuit in segments I and II. (c) Classical lumped-element band-pass circuit. We transfer the  $Z_{\lambda/4}$  line and the input source  $Z_0 = 50 \Omega$  into  $Z'_0$ . Additionally,  $Z_{\lambda/2}$  is transferred into a parallel LC circuit ( $Z_{parallel}$ ). The characteristic impedance values in each segment (I–IV) relate to a given prototype coefficient set  $g_i$  ( $i = 0, \dots, 3$ ) [see Eqs. (A25)–(A28)].

$I_L = CV_R = -iJ_i V_R$ , leading to

$$Y_L Y_R = -J_s^* J_i. \quad (\text{A14})$$

We then transform the admittance from right to left as shown in Fig. 6(b):

$$Y_R(-\omega_i) = Y_{idler}(-\omega_i) + \frac{1}{-i\omega_i L'_0}, \quad (\text{A15})$$

$$Y_L(\omega_s) = \frac{\alpha}{\omega_s \omega_i L_0'^2 Y_R(-\omega_i)}, \quad (\text{A16})$$

$$Y_{eff}(\omega_s) = Y_L(-\omega_i) + \frac{1}{i\omega_s L'_0},$$

$$= \frac{1}{i\omega_s L'_0} \left[ 1 + \frac{\alpha}{i\omega_i L_0' Y_{idler}^*(\omega_i) - 1} \right] \quad (\text{A17})$$

$$= \frac{1}{i\omega_s L_{eff}}, \quad (\text{A18})$$

where  $L_{eff}$  is the effective inductance associated to the modulated inductance  $L(t)$ , permitting complex values.

## 2. Three-stage impedance-transformer design

Signal amplification is achieved after transmission into a reflection-type device with negative resistance [40]. Appendix A1 demonstrated that a simplified complex inductance could represent the modulated inductance,

possibly offering negative resistance under a proper circuit design and pump condition. Here, we will examine the parametric amplifiers in synthesized impedance-matching networks of our circuit, as depicted in Fig. 7, following Ref. 38.

Beginning with the three-stage impedance-transformer amplification circuit in Fig. 1(a), containing transmission lines of specific lengths corresponding to a wavelength  $\lambda$ , we substitute  $L(t)$  with  $L_{eff}$  and replace  $L_{eff}$  again with an inductance in parallel with a resistor of value  $-R_{NR}$  with  $R_{NR} > 0$ , depicted in Fig. 7(a). Our objective is to derive an equivalent lumped-element band-pass network, including a source resistance of  $Z'_0$ , two resonators (a series and a parallel LC circuit), and a negative resistance,  $-R'_{NR}$ , as shown in Fig. 7(c).

We start by examining the impedance seen through a transmission line toward a load  $Z_L$  [51]:

$$Z_{tl \rightarrow L}(\omega) = Z_{tl} \frac{Z_L + iZ_{tl} \tan\left(\frac{\omega}{v_p} l\right)}{Z_{tl} + iZ_L \tan\left(\frac{\omega}{v_p} l\right)}, \quad (\text{A19})$$

where the transmission line has impedance  $Z_{tl}$  and length  $l$ , and  $v_p$  denotes the phase velocity. When a frequency  $\omega$  is close to their fundamental-mode frequency  $\omega_0 = 2\pi v_p / \lambda$ , and  $l$  is equal to  $\lambda/2$  or  $\lambda/4$ , we employ the following approximation:

$$\tan\left(\frac{\omega}{v_p} l\right) = \begin{cases} \frac{\pi \delta \omega}{\omega_0} = \pi \varepsilon & \text{for } l = \frac{\lambda}{2} \\ -\frac{2\pi \omega_0}{\delta \omega} = -\frac{2\pi}{\varepsilon} & \text{for } l = \frac{\lambda}{4}, \end{cases} \quad (\text{A20})$$

where  $\delta \omega = \omega - \omega_0$  and a normalized dimensionless parameter  $\varepsilon = \delta \omega / \omega_0$ .

Next, taking the limit of  $\delta \omega \rightarrow 0$  in Eq. (A19) for a quarter-wavelength transmission line, we obtain  $Z_{\lambda/4 \rightarrow L} = Z_{tl}^2 / Z_L$ , which is known as the impedance inverter [51]. Similarly, we apply the same rule for segment I and II in Fig. 7(a), where the impedance seen through the  $Z_{Kl, \lambda/4}$  line toward the right-side parallel RLC circuit with an impedance  $Z_{NR}$  and  $R_{NR}$  is equivalent to a series RLC circuit with  $R'_{NR} = Z_{Kl, \lambda/4}^2 / R_{NR}$  and a new series-LC impedance  $Z'_{NR} = Z_{Kl, \lambda/4}^2 / Z_{NR}$ .

Third, our goal is to match the  $Z_{\lambda/2}$  line [Fig. 7(b)] to an equivalent parallel LC circuit with impedance  $Z_{parallel}$  [Fig. 7(c)]. In particular, we calculate the impedance seen through the  $Z_{\lambda/2}$  line toward the  $Z_{\lambda/4}$  line and  $Z_0$ . The impedance seen through the  $Z_{\lambda/4}$  line toward the left-side  $Z_0$  in segment IV is given by

$$Z_{IV} = Z_{\lambda/4 \rightarrow Z_0} \approx \frac{\frac{Z_{\lambda/4}^2}{Z_0} + iZ_{\lambda/4} \frac{\pi \varepsilon}{2}}{1 + i \frac{Z_{\lambda/4} \pi \varepsilon}{Z_0}} = \frac{Z'_0 + i \frac{\pi \varepsilon}{2} Z_{\lambda/4}}{1 + i \frac{\pi \varepsilon}{2} \frac{Z_{\lambda/4}}{Z_0}}, \quad (\text{A21})$$

where we realize the source  $Z'_0 = Z_{\lambda/4}^2 / Z_0$  in Fig. 7(c). Next, the impedance seen from the  $Z_{\lambda/2}$  line in seg-

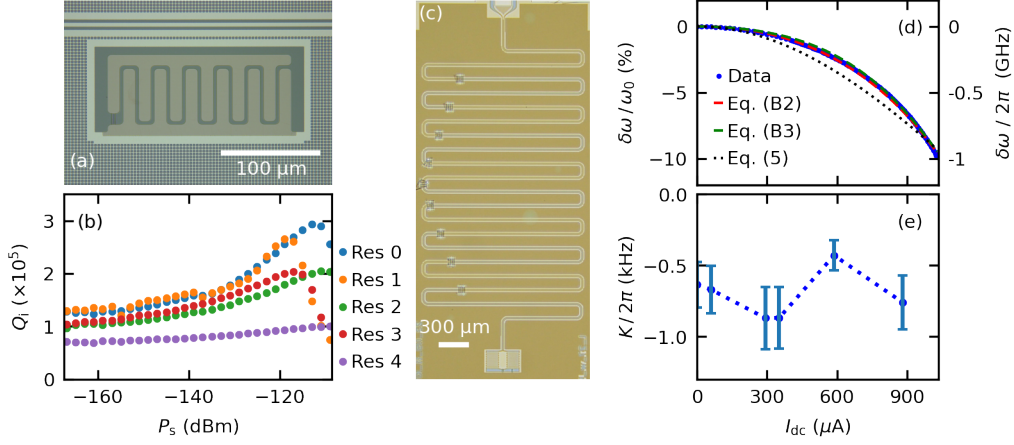


FIG. 8. (a) Optical image of a lumped-element LC resonator with a nanowire to calibrate the internal quality factor  $Q_i$ . (b)  $Q_i$  as a function of the signal power  $P_s$ . At the single-photon regime, we observe  $Q_i$  around  $10^5$  giving evidence that extra fabrication steps maintain the same quality of thin NbTiN films. (c) Single-pole kinetic-inductance parametric amplifier. Ten  $\lambda/4$  CPWs reduce the coupling between the nonlinear resonator to the 50- $\Omega$  port. Unlike the device in (a), neither aluminum covers the ground nor the transmission lines and the capacitor in (c). (d) Resonance-frequency shift  $\delta\omega$  vs dc bias current  $I_{dc}$  of the device shown in (c). Fits from Eqs. (B2), (B3) and (6) are plotted together. (e) Kerr coefficient  $K$  vs  $I_{dc}$ .

ment III toward segment IV is

$$\begin{aligned} Z_{\lambda/2 \rightarrow IV} &\approx Z_{\lambda/2} \frac{Z_{IV} + i\pi\varepsilon Z_{\lambda/2}}{Z_{\lambda/2} + i\pi\varepsilon Z_{IV}} \\ &\approx Z_{\lambda/2} \frac{Z'_0 + j\frac{\pi\varepsilon}{2} (Z_{\lambda/4} + 2Z_{\lambda/2})}{Z_{\lambda/2} + j\frac{\pi\varepsilon}{2} \left( \frac{Z_{\lambda/4} Z_{\lambda/2}}{Z_0} + 2Z'_0 \right)}. \end{aligned} \quad (\text{A22})$$

On the other hand, the impedance of the parallel RLC [in segments III and IV in Fig. 7(c)] is approximated as

$$\begin{aligned} Z_{\text{RLC}}^{-1} &= \frac{1}{Z'_0} - \frac{1}{iZ_{\text{parallel}}} \left\{ 1 + \varepsilon - \frac{1}{1 + \varepsilon} \right\} \\ &\approx \frac{1}{Z'_0} + i\frac{2\varepsilon}{Z_{\text{parallel}}}. \end{aligned} \quad (\text{A23})$$

In the limit of a small  $\delta\omega$ ,  $Z_{\lambda/2 \rightarrow IV}$  equals  $Z_{\text{RLC}}$ . By equating their imaginary components, we derive

$$Z_{\lambda/2}^2 + Z_{\lambda/2} \left( \frac{Z_{\lambda/4}}{2} - \frac{Z_{\lambda/4} Z'_0}{2Z_0} + \frac{Z_0'^2}{\pi} \frac{2}{Z_{\text{parallel}}} \right) - Z_0'^2 = 0. \quad (\text{A24})$$

To determine  $Z_{\text{parallel}}$ ,  $Z_{\lambda/4}$  and  $Z_{\lambda/2}$ , it is essential to select a prototype coefficient set  $\{g_i\}$  ( $i = 0, \dots, 3$ ) for a particular gain and ripples [38].  $g_0$ – $g_3$  correspond to the negative resistance ( $R'_{\text{NR}}$ ), series LC (with an impedance of  $Z'_{\text{NR}}$ ), parallel LC (with an impedance of  $Z_{\text{parallel}}$ ), and the load resistance ( $Z'_0$ ), respectively. The impedance set of segments I–IV is constructed according to a reference

impedance  $Z_{\text{ref}}$  [40]:

$$Z_{\text{ref}} = g_0 R'_{\text{NR}} = R'_{\text{NR}}, \quad (\text{A25})$$

$$Z'_{\text{NR}} = \frac{g_1}{\varepsilon} Z_{\text{ref}}, \quad (\text{A26})$$

$$\frac{1}{Z_{\text{parallel}}} = \frac{g_2}{\varepsilon} \frac{1}{Z_{\text{ref}}}, \quad (\text{A27})$$

$$Z'_0 = g_3 Z_{\text{ref}} = \frac{Z_{\lambda/4}^2}{Z_0}. \quad (\text{A28})$$

Utilizing the coefficients from Ref. 40, namely:

$$\{g_0, g_1, g_2, g_3\} = \{1, 0.408, 0.234, 1.106\}, \quad (\text{A29})$$

and setting  $\varepsilon = \delta\omega/\omega_0 = 500/8000$ ,  $Z_{\text{NR}} = 60 \Omega$ , and  $Z_{\text{KI}, \lambda/4} = 180 \Omega$ , we compute  $Z_{\text{ref}} = 82.7 \Omega$ ,  $Z_{\lambda/4} = 67.6 \Omega$ , and  $Z_{\text{parallel}} = 220.9 \Omega$ . Thereafter, solving Eq. (A24) yields  $Z_{\lambda/2} = 33.9 \Omega$ . Note that these parameters might not be ideal due to potential inaccuracies from the  $\tan(\omega l/v_p)$  approximation.

## Appendix B: NbTiN properties

Our fabrication process includes ion-milling to create the galvanic contacts of Al with NbTiN and wet etching of Al to expose NbTiN, possibly introducing losses. To evaluate these losses, we designed five similar lumped-element resonators with resonances near 8.5 GHz. Each device incorporates a nanowire inductor bridging two NbTiN pads, as illustrated in Fig. 8(a). The transmission lines and the ground plane are coated with thick Al, whereas the Al layer that covers the resonator pads is selectively eliminated. We measure these resonators in a

millikelvin environment. The internal quality factor  $Q_i$  vs the signal power  $P_s$  is shown in Fig. 8(b). When  $P_s$  is low,  $Q_i$  is approximately  $10^5$ .  $Q_i$  is enhanced as  $P_s$  increases due to the saturation of two-level systems responsible for dielectric loss [57]. This confirms the preservation of good quality in NbTiN films after the ion-milling and the wet-etching processes. Notably, flux-trapping holes all over the ground plane [Fig. 3(d)] are critical for enhancing  $Q_i$ ; without these holes,  $Q_i$  fell below  $10^4$ .

Current sensitivity  $I_*$  is extracted from the resonance-frequency response while varying the injection of the dc current  $I_{dc}$  in a different device as shown in Fig. 8(c). The design incorporates  $N = 10$  sections of stepped-impedance  $\lambda/4$  transmission-line filters with alternating high ( $Z_H$ ) and low ( $Z_L$ ) impedance sections, connected in series to an LC resonator comprised of a nanowire NbTiN and an interdigitated capacitor. The external quality factor  $Q_e$  is derived to be [28]

$$Q_e = \left( \frac{Z_H}{Z_L} \right)^{2N} \frac{\pi Z_0}{4Z_{NR}}. \quad (\text{B1})$$

We choose  $N = 5$ ,  $Z_H = 90 \Omega$ ,  $Z_L = 35 \Omega$  and  $Z_{NR} = 60 \Omega$  expecting  $Q_e = 8269$  and measure  $Q_e = 7500$ , in good agreement with the theory. To enhance the accuracy of resonance-frequency measurement,  $Q_e$  is designed to be close to  $Q_i$ .

The resonance frequency shift  $\delta\omega$  vs  $I_{dc}$  is shown in Fig. 8(d). However, we realize that the fit to Eq. (6) (black dotted line) with only the quadratic term fails to match our measurement results. Taking into account the quartic term  $I_{*4}$  [25], we write

$$L_k(I_{dc}) = L_{k0} \left[ 1 + \left( \frac{I_{dc}}{I_{*2}} \right)^2 + \left( \frac{I_{dc}}{I_{*4}} \right)^4 \right]. \quad (\text{B2})$$

From the fit, we obtain  $I_{*2} = 3.25$  mA and  $I_{*4} = 1.7$  mA, while  $I_c = 1.15$  mA is measured by increasing  $I_{dc}$  until the superconductivity breaks down. This yields  $I_c/I_{*2} = 0.35$ , which is close to the theoretical limit of 0.42 [25].

It is worth mentioning another expression  $L_k(I)$ , which discusses the behavior of Cooper pairs under both ac and dc currents:

$$L_k(I_{dc}) = \frac{L_{k0}}{[1 - (I_{dc}/I_{**})^n]^{\frac{1}{n}}}, \quad (\text{B3})$$

where  $n = 2.21$  [45]. From this expression, we obtain  $I_{**} = 1.65$  mA and  $I_c/I_{**} = 0.7$ , which are in good agreement with the theory suggesting  $I_c \approx 0.66I_{**}$ . Eq. (B3) is useful since it has only one fitting parameter  $I_{**}$ .

We determine the surface impedance per square  $L_{sq} = L_{k0}(w/l)$  by comparing the measured  $\lambda/2$  NbTiN CPW resonance to the simulations performed in COMSOL, yielding  $L_{sq} = 6.7$  pH/square for the 20-nm-thick film. This result is consistent with the measurements of  $L_k(I_{dc})$ , assuming a fixed geometric inductance  $L_g \approx 200$  pH according to COMSOL simulations.

### Appendix C: Kinetic-inductance nonlinearity

In this Appendix, we will express the inductance modulation amplitude  $\delta L$  in terms of the pump current  $I_p$  and  $I_*$  using the Hamiltonian. For simplicity, we begin with Eq. (6) while excluding the quartic term associated with  $I_{*4}$ . For a parametric oscillator comprised of a parallel inductor and a capacitor, the Lagrangian is given by

$$\begin{aligned} \mathcal{L} &= \frac{1}{2} L_k(I) \dot{q}^2 - \frac{q^2}{2C} \\ &= \frac{1}{2} L_{k0} \dot{q}^2 \left( 1 + \left( \frac{I_{dc}}{I_*} \right)^2 + \frac{2I_{dc}\dot{q}}{I_*^2} + \left( \frac{\dot{q}}{I_*} \right)^2 \right) - \frac{q^2}{2C}, \end{aligned} \quad (\text{C1})$$

where  $I = I_{dc} + I_{ac}$  and  $I_{ac} = \dot{q}$  represents the ac current across the inductor and  $q$  is the charge on the capacitors. To simplify the notation, we introduce  $L_I = L_{k0}(1 + i_{dc}^2)$ , where  $i_{dc} = I_{dc}/I_*$ .

The conjugate momentum of  $q$  is

$$\begin{aligned} \Phi &= \frac{\partial \mathcal{L}}{\partial \dot{q}} \\ &= \frac{1}{2} L_I \left( 2\dot{q} + \frac{6i_{dc}}{1 + i_{dc}^2} \frac{\dot{q}^2}{I_*} + \frac{4\dot{q}}{1 + i_{dc}^2} \left( \frac{\dot{q}}{I_*} \right)^2 \right). \end{aligned} \quad (\text{C2})$$

To express  $\dot{q}$  in  $\Phi$ , we assume  $I_* \gg \dot{q}$  in the sense that  $I_* > I_c > I_{dc} + \dot{q}$  such that the second and the third terms in Eq. (C2) are much smaller than the first term. We rearrange Eq. (C2) into

$$\begin{aligned} \dot{q} &= \frac{\Phi}{L_I} - \frac{3i_{dc}\dot{q}^2}{(1 + i_{dc}^2)I_*} - \frac{2\dot{q}^3}{(1 + i_{dc}^2)I_*^2} \\ &= I_\Phi - \mathcal{A}\dot{q}^2 - \mathcal{B}\dot{q}^3, \end{aligned} \quad (\text{C3})$$

where  $I_\Phi = \frac{\Phi}{L_I}$ ,  $\mathcal{A} = \frac{3i_{dc}}{(1 + i_{dc}^2)I_*}$ , and  $\mathcal{B} = \frac{2}{(1 + i_{dc}^2)I_*^2}$ . We iteratively substitute  $\dot{q}$  back into the right-hand side (RHS) of Eq. (C3) until RHS contains only powers of  $I_\Phi$  up to the quartic order ( $I_\Phi^4$ ) and yield

$$\begin{aligned} \dot{q}^2 &\approx I_\Phi^2 - 2\mathcal{A}I_\Phi^3 - 2\mathcal{B}I_\Phi^4 + 5\mathcal{A}^2I_\Phi^4, \\ \dot{q}^3 &\approx I_\Phi^3 - 3\mathcal{A}I_\Phi^4, \\ \dot{q}^4 &\approx I_\Phi^4. \end{aligned} \quad (\text{C4})$$

The Hamiltonian  $\mathcal{H}$  is obtained through Legendre transformation:

$$\begin{aligned} \mathcal{H} &= \Phi\dot{q} - \mathcal{L} \\ &\approx \frac{1}{2} L_I \left( I_\Phi^2 - \frac{2}{3}\mathcal{A}I_\Phi^3 + \mathcal{A}^2I_\Phi^4 - \frac{1}{2}\mathcal{B}I_\Phi^4 \right) + \frac{q^2}{2C}. \end{aligned} \quad (\text{C5})$$

Separating  $\mathcal{H}$  to a linear harmonic-oscillator Hamiltonian  $\mathcal{H}_0$  and a perturbed nonlinear Hamiltonian  $\mathcal{H}_1$ , we

find

$$\mathcal{H}_0 = \frac{\Phi^2}{2L_I} + \frac{q^2}{2C}, \quad (\text{C6})$$

and

$$\begin{aligned} \mathcal{H}_1 &= \frac{1}{2}L_I \left( -\frac{2}{3}\mathcal{A}I_\Phi^3 + \mathcal{A}^2I_\Phi^4 - \frac{1}{2}\mathcal{B}I_\Phi^4 \right) \\ &= -\frac{i_{\text{dc}}}{(1+i_{\text{dc}}^2)L_I^2I_*} \Phi^3 + \frac{-1+8i_{\text{dc}}^2}{2(1+i_{\text{dc}}^2)^2L_I^3I_*^2} \Phi^4. \end{aligned} \quad (\text{C7})$$

Subsequently, we treat the strong pump  $I_p(t)$  classically, while the remaining degrees of freedom are treated quantum mechanically in  $\Phi$ :

$$\Phi = \Phi_p + \hat{\Phi} = L_I|I_p| \cos(\omega_p t + \varphi_p) + \hat{\Phi}. \quad (\text{C8})$$

Here, the quantum operator  $\hat{\Phi}$  and  $\hat{q}$  are defined by the new linear-oscillator Hamiltonian  $\mathcal{H}'_0$  ignoring classical terms:

$$\hat{\Phi} = \sqrt{\frac{\hbar Z_{\text{NR}}}{2}} (\hat{a}^\dagger + \hat{a}), \quad (\text{C9})$$

$$\hat{q} = i\sqrt{\frac{\hbar}{2Z_{\text{NR}}}} (\hat{a}^\dagger - \hat{a}), \quad (\text{C10})$$

$$\mathcal{H}'_0 = \hbar\omega_0 \left( \hat{a}^\dagger \hat{a} + \frac{1}{2} \right), \quad (\text{C11})$$

where the characteristic impedance of the nonlinear resonator  $Z_{\text{NR}} = \sqrt{L_I/C}$ , the resonance frequency  $\omega_0 = 1/\sqrt{L_I C}$ , and the lowering operator  $\hat{a}$  are introduced. In the Heisenberg picture of  $\mathcal{H}'_0$ , the operator  $\hat{a}$  oscillates in time and  $\hat{a} = \hat{a}(0)e^{-i\omega_0 t}$ . Substituting Eq. (C8) back into Eq. (C7) and assuming  $\omega_p \approx 2 \times \omega_0$ , we reformulate  $\mathcal{H}_1$  by omitting all fast-rotating and constant terms, and obtain:

$$\begin{aligned} \frac{\mathcal{H}_1}{\hbar} &= -\frac{3}{4} \frac{i_{\text{dc}}}{(1+i_{\text{dc}}^2)} \frac{|I_p|Z_{\text{NR}}}{L_I I_*} \left( a^\dagger a^\dagger e^{-i(\omega_p t + \varphi_p)} + \text{h.c.} \right) \\ &+ \frac{3}{4} \frac{8i_{\text{dc}}^2 - 1}{(1+i_{\text{dc}}^2)^2} \frac{\hbar Z_{\text{NR}}^2}{L_I^3 I_*^2} (a^\dagger a)^2 \\ &+ \frac{3}{2} \frac{8i_{\text{dc}}^2 - 1}{(1+i_{\text{dc}}^2)^2} \frac{Z_{\text{NR}}|I_p|^2}{L_I I_*^2} a^\dagger a. \end{aligned} \quad (\text{C12})$$

We define the amplification coefficient  $\xi_3$  and Kerr strength  $K$  for the cubic and quartic terms of  $a$ , respectively, and the pump-induced shift  $\delta_p$  as

$$\xi_3 = -\frac{3}{2} \frac{I_{\text{dc}}|I_p|}{(I_*^2 + I_{\text{dc}}^2)} \omega_0 e^{-i\varphi_p}, \quad (\text{C13})$$

$$K = \frac{3}{4} \frac{8I_{\text{dc}}^2 - I_*^2}{(I_*^2 + I_{\text{dc}}^2)^2} \frac{\hbar\omega_0^2}{L_I}, \quad (\text{C14})$$

and

$$\delta_p = \frac{3}{2} \frac{8I_{\text{dc}}^2 - I_*^2}{(I_*^2 + I_{\text{dc}}^2)^2} \omega_0 |I_p|^2. \quad (\text{C15})$$

The full Hamiltonian becomes:

$$\mathcal{H}/\hbar = \left( \omega_0 - \frac{K}{2} + \delta_p \right) \hat{a}^\dagger \hat{a} + \frac{\xi_3}{2} \hat{a}^\dagger \hat{a}^\dagger + \frac{\xi_3^*}{2} \hat{a} \hat{a} + K \hat{a}^\dagger \hat{a}^\dagger \hat{a} \hat{a} \quad (\text{C16})$$

In Fig. 8(e),  $K$  is determined by sending a strong tone at the resonance of the device shown in Fig. 8(c), while a weak tone is applied to measure the shift of the resonance frequency. Because of the error bar, the dependence of  $K$  on  $I_{\text{dc}}$  is not distinctly observable. Given  $I_* = 3.25$  mA, we anticipate  $K/2\pi \approx 13$  Hz, a value that deviates from our observations. Nevertheless,  $K$  is still 2 to 3 orders of magnitude smaller than a typical JJ-based PA. A small  $K$  is the key to achieving high  $P_{1\text{dB}}$  [41, 42].

As we did in Appendix A 1, we assume that voltage and current contain only the dominant terms of  $\omega_s$ ,  $\omega_i$ , and  $\omega_p$  and obtain the following:

$$V = \frac{1}{2} (V_s e^{i\omega_s t} + V_i e^{i\omega_i t} + V_p e^{i\omega_p t} + \text{c.c.}), \quad (\text{C17})$$

and

$$\dot{q} = \frac{1}{2} (I_s e^{i\omega_s t} + I_i e^{i\omega_i t} + I_p e^{i\omega_p t} + \text{c.c.}). \quad (\text{C18})$$

Note that voltage  $V$  relates to  $\Phi$  (and  $\dot{q}$ ) as [58]

$$\Phi(t) = \int_{-\infty}^t V(t') dt'. \quad (\text{C19})$$

Under the assumption of  $K \ll \xi_3$ , from Eq. (C2) we obtain

$$\begin{aligned} V &= L_I \left( \ddot{q} + \frac{6i_{\text{dc}}}{1+i_{\text{dc}}^2} \frac{\dot{q}\ddot{q}}{I_*} + \frac{6}{1+i_{\text{dc}}^2} \frac{\dot{q}^2\ddot{q}}{I_*^2} \right) \\ &\approx L_I \left( \ddot{q} - \frac{2\xi_3}{\omega_0 I_*} \dot{q}\ddot{q} \right). \end{aligned} \quad (\text{C20})$$

Substituting

$$\ddot{q} = i\omega_s \frac{I_s}{2} e^{i\omega_s t} + i\omega_i \frac{I_i}{2} e^{i\omega_i t} + i\omega_p \frac{I_p}{2} e^{i\omega_p t} + \text{c.c.} \quad (\text{C21})$$

into Eq. (C20) and separating different frequency terms, we obtain

$$\begin{pmatrix} V_s \\ V_i^* \\ V_i \\ V_s^* \end{pmatrix} = \begin{pmatrix} \mathbf{Z} & \mathbf{0} \\ \mathbf{0} & \mathbf{Z}^* \end{pmatrix} \begin{pmatrix} I_s \\ I_i^* \\ I_i \\ I_s^* \end{pmatrix}, \quad (\text{C22})$$

where

$$\mathbf{Z} = iL_I \begin{pmatrix} \omega_s & \frac{\omega_s}{2\omega_0} \xi_3^* \\ -\frac{\omega_i}{2\omega_0} \xi_3 & -\omega_i \end{pmatrix} \quad (\text{C23})$$

Comparing to the Z-matrix of Eq. (A4), we obtain

$$\begin{aligned} L_I &= L_k(I_{dc}) \\ \delta L &= \frac{3}{2} \frac{I_{dc} I_p^*}{I_*^2 + I_{dc}^2} L_I \\ \alpha &= \frac{9}{16} \left( \frac{I_{dc} |I_p|}{I_*^2 + I_{dc}^2} \right)^2 = \frac{1}{4} \frac{|\xi_3|^2}{\omega_0^2}. \end{aligned} \quad (\text{C24})$$

For comparison, a single JJ exhibits [38]

$$L_J(I) = \frac{L_{J0}}{\sqrt{1 - \frac{I^2}{I_{J,c}^2}}} \approx L_{J0} \left( 1 + \frac{I^2}{2I_{J,c}^2} \right) \quad (\text{C25})$$

and

$$\alpha \approx \frac{1}{4} \left( \frac{I_{dc} |I_p|}{I_{J,c}^2 + I_{dc}^2} \right)^2. \quad (\text{C26})$$

Since KI materials typically have  $I_*$  values 2–3 orders of magnitude higher than  $I_{J,c}$ , they require proportionally higher pump currents to reach the same  $\alpha$ . We choose nanowire NbTiN inductors (20-nm-thick and 250-nm-wide) to reduce  $I_*$  to the order of milliamperes, further mitigating potential heating.

#### Appendix D: Negative-resistance simulation

Here, we simulate the reflection coefficient  $S_{11}$  of our three-stage impedance-transformer circuit with a negative resistance by direct calculations based on Eqs. (3) and (A19). Since  $|\xi_3|$ , which is proportional to pump current  $|I_p|$ , provides a clear physical meaning for the strength of amplification, we plot  $|\xi_3|$  vs gain instead of  $R_{NR}$  vs gain. An example of the gain profile as a function of  $\omega_s$  and  $|\xi_3|$  in an ideal 50- $\Omega$  environment is shown in Fig. 9(a). In Fig. 9(b), the blue curve with two gain peaks at the optimal point  $|\xi_3|/2\pi = 1.5$  GHz, indicating a two-pole system, overcomes the gain–bandwidth product and matches the measurement in Fig. 3(c). A single peak occurs when  $|\xi_3|/2\pi > 1.5$  GHz [orange curve in Fig. 9(b)] showing a narrower bandwidth than the blue curve.

In Fig. 9(c), we simulate the process depicted in Fig. 3(e) by sweeping  $\omega_p$  and  $I_{dc}$ . Since superconductivity breakdowns are observed at large  $|I_p|$ , we increase  $|\xi_3|$  until  $G_s$  reaches 40 dB and report the maximum bandwidth  $\Delta\omega$  for each  $(\omega_p, I_{dc})$  pair at 17-dB gain. At different  $I_{dc}$ , we find that the maximum  $\Delta\omega$  happens when  $(\omega_p/2)/2\pi$  is near 8.45 GHz corresponding to the res-

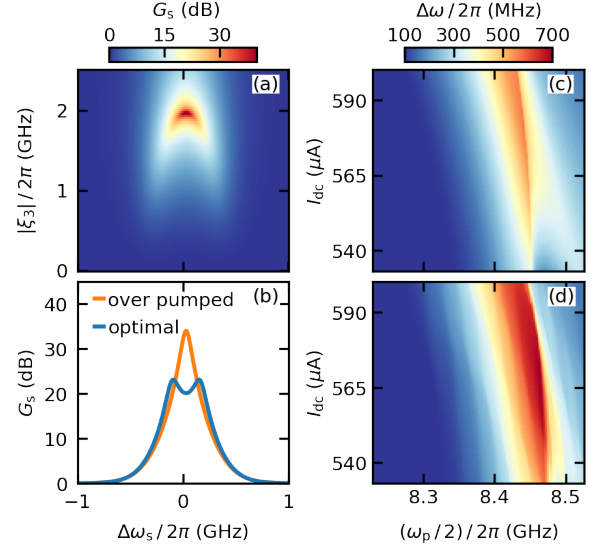


FIG. 9. Negative-resistance-circuit simulations. (a)  $G_s$  as a function of  $\Delta\omega_s = \omega_s - 2\omega_p$  and the amplification strength  $|\xi_3|$ . (b) Gain spectra at two different  $|\xi_3|$ . At an optimal  $|\xi_3|$ , we observe two peaks breaking the gain–bandwidth product but only a single peak when it is over-pumped. (c) Simulation of the bandwidth at 17-dB gain as a function of  $I_{dc}$  and  $\omega_p$  under an ideal 50  $\Omega$ . (d) Enhanced bandwidth under a non-ideal input conditions  $Z_{env}$  using Eq. (8).

onance of  $\lambda/2$  line. This contrasts with measurement data where the resonance of our  $Z_{\lambda/2}$  line shifts by tens of megahertz depending on  $I_{dc}$  due to a small kinetic inductance  $L_k$  in aluminum.

The PA interacting with the non-ideal environment  $Z_{env}$  is analogous to a  $N$ -pole system ( $N > 2$ ). The additional modes arise from standing waves in the coaxial cable, which can either enhance or reduce the bandwidth under certain conditions. From Eq. (8),  $Z_{env}(2\pi \times 8.45 \text{ GHz}) = 51 \Omega$  might cause constructive interference as simulated in Fig. 9(d), where we observe a bandwidth increased by around 20% compared to an ideal 50- $\Omega$  case.

#### Appendix E: Comparison to Roy’s model

In Appendix A 2, we demonstrated that the three-stage impedance-transformer circuit allows us to use high-impedance parametric oscillators. This section systematically compares our circuit to the conventional circuit lacking the  $Z_{KI,\lambda/4}$  line [17]. We perform a brute-force search over all feasible combinations of the design parameters including  $Z_{\lambda/4}$ ,  $Z_{\lambda/2}$ ,  $Z_{NR}$ , and  $\omega_p$ .

First, in our circuit, we set fixed values for the nonlinear-oscillator resonance frequency  $\omega_0/2\pi = 8$  GHz,  $\lambda$  corresponding to  $\omega_0$ , and  $Z_{KI,\lambda/4} = 150 \Omega$ . Then, we sweep multiple parameters across specific ranges:  $Z_{\lambda/4} \in [50 \Omega, 100 \Omega]$ ,  $Z_{\lambda/2} \in [30 \Omega, 50 \Omega]$ ,  $(\omega_p/2)/2\pi \in [7.5 \text{ GHz}, 8.5 \text{ GHz}]$  and  $Z_{NR} \in [50 \Omega, 100 \Omega]$ . We sim-

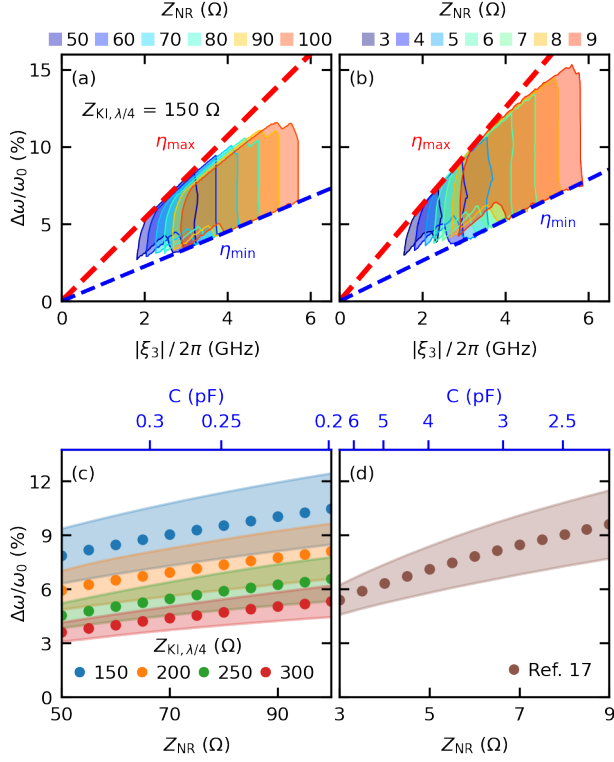


FIG. 10. Comparison of our three-stage impedance-transformer and the conventional circuit in Ref. 17. (a) Bandwidth  $\Delta\omega$  as a function of  $|\xi_3|$  in our circuit, categorized by  $Z_{NR}$ . Two dashed lines represent the maximum (red) and minimum (blue) pump efficiency  $\eta = \Delta\omega/|\xi_3|$ . We observe that maximum  $\eta$  has a negative correlation with  $Z_{NR}$ . (b) Bandwidth  $\Delta\omega$  as a function of  $|\xi_3|$  using the conventional circuit [17]. The same brute-force search process as described in (a). (c) Average and the standard deviation of  $\Delta\omega$  as a function of  $Z_{NR}$  using our circuit. On the upper horizontal axis, we show the required capacitance. (d) Average and the standard deviation of  $\Delta\omega$  as a function of  $Z_{NR}$  using the conventional circuit. For  $\Delta\omega/\omega_0 = 6\%$ , our circuit requires only  $\sim 400$  fF compared to 5 pF in the conventional circuit.

ulate the response similar to Fig. 9(a) for each parameter set  $\{Z_{\lambda/4}, Z_{\lambda/2}, \omega_p, Z_{NR}\}$ . During the increase of  $|\xi_3|$  until the gain  $G_s(|\xi_3|)$  surpasses 40 dB, we record the maximum  $\Delta\omega$  in the condition that  $G_s$  with a correspondingly optimal  $|\xi_3|$  shows more than 17-dB gain with ripples under 3 dB and two local maxima, resembling a two-pole system. For instance, in Fig. 9(a),  $|\xi_3|/2\pi$  is elevated to about 2 GHz, with results showing maximum  $\Delta\omega/2\pi \approx 420$  MHz and optimal  $|\xi_3|/2\pi = 1.5$  GHz for the given parameter set. The enclosed area, categorized by  $Z_{NR}$  using a consistent color as shown in Fig. 10(a), indicates the achievable maximum  $\Delta\omega$  and optimal  $|\xi_3|$ . As  $Z_{NR}$  rises, the corresponding area shifts to the right, implying larger  $|\xi_3|$  is needed for larger  $Z_{NR}$ .

The pump efficiency  $\eta$ , defined as  $\eta = \Delta\omega/|\xi_3|$ , is important in indicating how the pump power transfers to

the bandwidth. Dashed lines indicate the maximum (red) and minimum (blue)  $\eta$ , revealing that low  $Z_{NR}$  has a slightly better pump efficiency.

In Fig. 10(b), we extend our analysis to the conventional circuit [17], revealing that the allowed  $Z_{NR} \in [3 \Omega, 9 \Omega]$  is approximately ten times smaller. On the other hand, the pump efficiency is slightly better than our proposed circuit. In Fig. 10(c), we compare  $\Delta\omega/\omega_0$  as a function of  $Z_{NR}$  with various  $Z_{KI,\lambda/4}$ . Dots are the average of all possible  $\Delta\omega$ , and the area shows the standard deviation. All  $Z_{KI,\lambda/4}$  behave similarly that  $\Delta\omega$  raises with  $Z_{NR}$ . Since  $|\xi_3|$  is proportional to  $|I_p|$  (or the square root of the pump power), if the pump power is constrained by the function generator or  $|\xi_3|$  is limited by the material's nature, selecting a smaller  $Z_{NR}$  or a larger  $Z_{KI,\lambda/4}$  is a viable strategy for designing PAs in our scheme.

It is worth mentioning that, given the theoretical limitation  $I_{dc} + |I_p| < I_c \lesssim 0.42I_*$  [25], we can derive the following inequality and calculate the upper limit of  $|\xi_3|$ :

$$\frac{|\xi_3|}{\omega_0} = \frac{3}{2} \frac{I_{dc}|I_p|}{(I_*^2 + I_{dc}^2)} \leq \frac{3}{2} \frac{(I_c - |I_p|)|I_p|}{5.7I_c^2 + (I_c - |I_p|)^2}, \quad (E1)$$

which yields maximum  $|\xi_3|/2\pi \approx 0.6$  GHz. In our circuit, the simulated maximum  $\eta = 0.21$  yields a maximum bandwidth of 120 MHz, which is much smaller than our measurement. Apparently, we underestimate  $|\xi_3|$ , and the precise form of  $L_k(I)$  should include higher-order terms and follow the analysis of both effects of dc and ac currents in Ref. 45, which is beyond the scope of this paper.

## Appendix F: System-noise calibration and experimental setup

This appendix describes the method for extracting the input-line attenuation  $A_{in}$  using a qubit. A qubit coupled to a waveguide with an external coupling rate  $\Gamma_{1,E}$  much larger than its internal decay rate  $\Gamma_{1,I}$  is a useful tool to calibrate the input power. Under a weak input coherent drive sent through the waveguide, the qubit absorbs a single photon and emits the photon in both directions with a  $\pi$  phase shift. The forward signal interferes destructively with the emission, causing a dip in  $|S_{21}|$  near the qubit frequency  $\omega_q$  [Fig. 11(a)]. On the contrary, with a strong input, the qubit can only absorb one photon before emitting it, and  $S_{21}$  approaches unity. Solving the master equation in the steady state with  $\hbar\omega \gg k_B T$ ,  $S_{21}$  is written as [49, 59]

$$S_{21}(\omega) = 1 - \frac{\Gamma_{1,E}}{2\Gamma_2} \frac{1 + i\frac{\Delta_q}{\Gamma_2}}{1 + \left(\frac{\Delta_q}{\Gamma_2}\right)^2 + \frac{\Omega_d^2}{\Gamma_1\Gamma_2}}, \quad (F1)$$

where  $\Delta_q = \omega - \omega_q$  is the detuning between the input and qubit frequencies,  $\Gamma_1 = \Gamma_{1,E} + \Gamma_{1,I}$  is the total decay

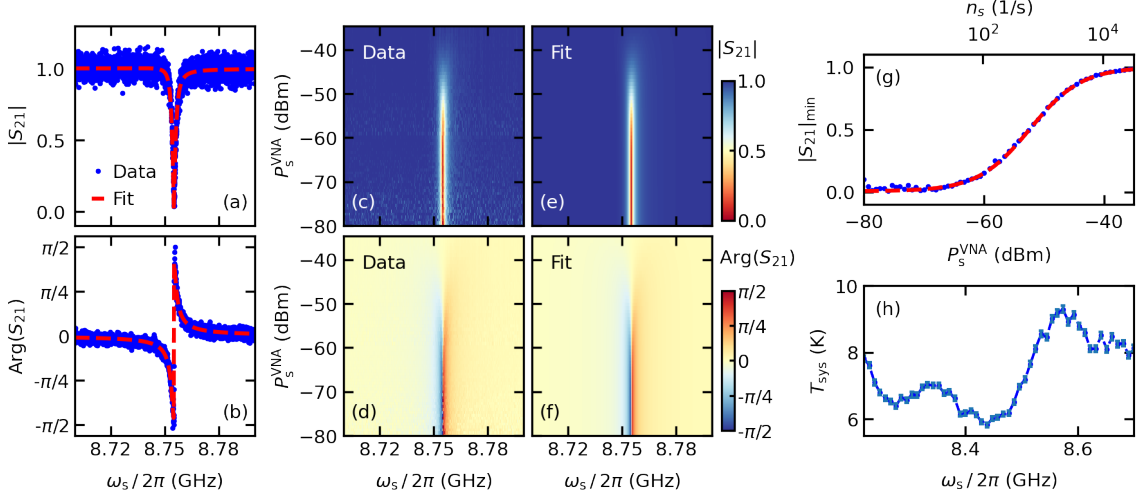


FIG. 11. Calibration of the signal power using a transmon qubit coupled to a transmission line. (a) Amplitude and (b) phase of the transmission coefficient  $S_{21}$  as a function of the signal frequency  $\omega_s$ . The data is taken at a low signal power from VNA,  $P_s^{\text{VNA}} = -75$  dBm. The red dashed lines are the fit to Eq. (F1). (c) and (d) Amplitudes and phase of  $S_{21}$  as a function of  $\omega_s$  and  $P_s^{\text{VNA}}$ . (e) and (f) Fits to (c) and (d). (g)  $|S_{21}|$  at the resonance frequency as a function of  $P_s^{\text{VNA}}$ . The top axis indicates the corresponding number of signal photons per second  $n_s$ . (h) System noise temperature  $T_{\text{sys}}$  vs  $\omega_s$ .

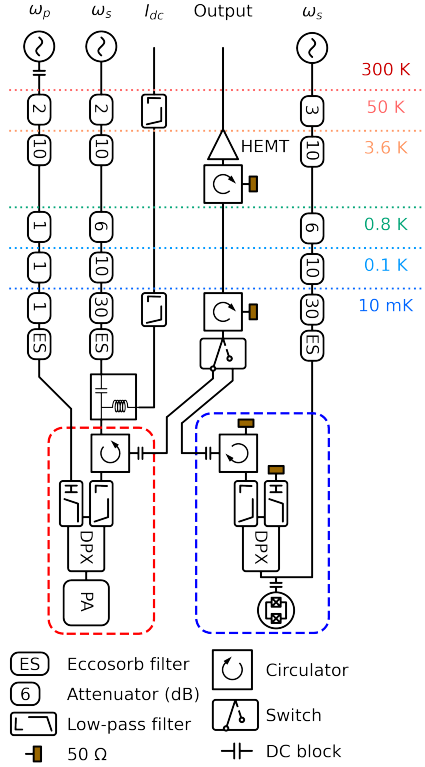


FIG. 12. Schematic of the cryogenic microwave-wiring setup. The PA and the transmon qubit share the same output chain via a microwave switch.

rate,  $\Gamma_2 = \Gamma_\phi + \Gamma_1/2$  is the dephasing rate, and  $\Gamma_\phi$  is the pure dephasing rate of the qubit. Here  $\Omega_d$  is the drive strength at the input signal power  $P_d$ , and

$$\Omega_d = \sqrt{\frac{2\Gamma_{1,E}P_d}{\hbar\omega_q}}. \quad (\text{F2})$$

In the case of  $\Gamma_1 \approx \Gamma_{1,E}$  or  $\Gamma_{1,E} \gg \Gamma_{1,I}$ , we fit the measured  $S_{21}$  across the power  $P_s^{\text{VNA}}$  sent from the vector network analyzer at room temperature to extract the input attenuation by  $A_{\text{in}} = P_s^{\text{VNA}}/P_d$ .

Measured  $S_{21}$  and its fit are shown in Figs. 11(c)–(f). From the fit, we extracted  $\Gamma_1/2\pi = 3.35 \pm 0.15$  MHz,  $\Gamma_\phi/2\pi = 1.06 \pm 0.11$  kHz, and  $\Omega_d/2\pi = 98.6 \pm 9.7$  kHz at  $P_s^{\text{VNA}} = -80$  dBm, resulting in  $A_{\text{in}} = -82 \pm 0.85$  dB. In Fig. 11(g), we show the minimum magnitude of  $S_{21}$  vs  $P_s^{\text{VNA}}$  at  $\Delta_q = 0$ . On the upper horizontal axis, the photon number per second,  $n_s = \Omega_d^2/2\Gamma_1$ , is shown, where the saturation starts at  $n_s \gg 1$  or  $P_s^{\text{VNA}} \approx -57$  dBm.

In Eq. (12), all variables except  $G_{\text{sys}}^{\text{eff}} = A_{23}G_{\text{sys}}$  are retrieved using a spectrum analyzer, and  $G_{\text{sys}}^{\text{eff}}$  is calculated via the equation  $P_s^{\text{VNA}}A_{\text{in}}G_sG_{\text{sys}}^{\text{eff}} = P_f$ , where  $P_f$  is the output power measured with the spectrum analyzer. As  $G_{\text{sys}}^{\text{eff}}$  only relates to post-PA components, its determination doesn't depend on the input line setup. Two input lines are thus utilized for the PA and qubit, sharing an output line, with only one microwave switch for signal routing to minimize the number of switches (typically there is another one placed before the PA and see Fig. 12 for our setup). As PA measurements are of the reflection type, the amplified signal undergoes attenuation by a diplexer and a circulator, which contributes to  $A_{23}$ . Therefore, this additional loss mechanism must be

accounted for in the qubit measurement chain, where a diplexer and a circulator are situated directly after the qubit sample holder. This ensures consistent  $A_{23}$  across both paths, presuming similar loss effects from these passive components. We perform saturation measurements

on a tunable qubit at different frequencies by flux biasing from 8.2 to 8.7 GHz to extract  $A_{in}(\omega)$ . In Fig. 11(h), assuming  $N_{sys} \gg N_3^{off}$ , the system noise temperature is expressed as  $T_{sys} = N_4^{off} \hbar\omega/k_B G_{sys}^{eff}$ , resulting in  $T_{sys}$  values between 5.9 and 9.2 K.

- 
- [1] R. Vijay, M. Devoret, and I. Siddiqi, Invited Review article: The Josephson bifurcation amplifier, *Review of Scientific Instruments* **80** (2009).
- [2] A. A. Clerk, M. H. Devoret, S. M. Girvin, F. Marquardt, and R. J. Schoelkopf, Introduction to quantum noise, measurement, and amplification, *Reviews of Modern Physics* **82**, 1155 (2010).
- [3] C. Macklin, K. O’Brien, D. Hover, M. Schwartz, V. Bolkhovskiy, X. Zhang, W. Oliver, and I. Siddiqi, A near-quantum-limited Josephson traveling-wave parametric amplifier, *Science* **350**, 307 (2015).
- [4] J. Aumentado, Superconducting parametric amplifiers: The state of the art in Josephson parametric amplifiers, *IEEE Microwave Magazine* **21**, 45 (2020).
- [5] J. Heinsoo, C. K. Andersen, A. Remm, S. Krinner, T. Walter, Y. Salathé, S. Gasparinetti, J.-C. Besse, A. Potočnik, A. Wallraff, *et al.*, Rapid high-fidelity multiplexed readout of superconducting qubits, *Physical Review Applied* **10**, 034040 (2018).
- [6] A. Bienfait, J. Pla, Y. Kubo, M. Stern, X. Zhou, C. Lo, C. Weis, T. Schenkel, M. Thewalt, D. Vion, *et al.*, Reaching the quantum limit of sensitivity in electron spin resonance, *Nature Nanotechnology* **11**, 253 (2016).
- [7] C. Eichler, A. Sigillito, S. A. Lyon, and J. R. Petta, Electron spin resonance at the level of  $10^4$  spins using low impedance superconducting resonators, *Physical Review Letters* **118**, 037701 (2017).
- [8] W. Vine, M. Savytskyi, A. Vaartjes, A. Kringhøj, D. Parker, J. Slack-Smith, T. Schenkel, K. Mølmer, J. C. McCallum, B. C. Johnson, *et al.*, In situ amplification of spin echoes within a kinetic inductance parametric amplifier, *Science Advances* **9**, eadg1593 (2023).
- [9] K. M. Backes, D. A. Palken, S. A. Kenany, B. M. Brubaker, S. Cahn, A. Droster, G. C. Hilton, S. Ghosh, H. Jackson, S. K. Lamoreaux, *et al.*, A quantum enhanced search for dark matter axions, *Nature* **590**, 238 (2021).
- [10] T. Braine, R. Cervantes, N. Crisosto, N. Du, S. Kimes, L. Rosenberg, G. Rybka, J. Yang, D. Bowering, A. Chou, *et al.*, Extended search for the invisible axion with the axion dark matter experiment, *Physical Review Letters* **124**, 101303 (2020).
- [11] S. V. Uchaikin, B. I. Ivanov, J. Kim, Ç. Kutlu, A. F. Van Loo, Y. Nakamura, S. Oh, V. Gkika, A. Matlashov, W. Chung, *et al.*, CAPP Axion Search Experiments with Quantum Noise Limited Amplifiers, in *Proceedings of the 29th International Conference on Low Temperature Physics (LT29)* (2023) p. 011201.
- [12] A. D. Córcoles, E. Magesan, S. J. Srinivasan, A. W. Cross, M. Steffen, J. M. Gambetta, and J. M. Chow, Demonstration of a quantum error detection code using a square lattice of four superconducting qubits, *Nature Communications* **6**, 6979 (2015).
- [13] Y. Zhao, Y. Ye, H.-L. Huang, Y. Zhang, D. Wu, H. Guan, Q. Zhu, Z. Wei, T. He, S. Cao, *et al.*, Realization of an error-correcting surface code with superconducting qubits, *Physical Review Letters* **129**, 030501 (2022).
- [14] B. Yurke, L. Corruccini, P. Kaminsky, L. Rupp, A. Smith, A. Silver, R. Simon, and E. Whittaker, Observation of parametric amplification and deamplification in a Josephson parametric amplifier, *Physical Review A* **39**, 2519 (1989).
- [15] M. Castellanos-Beltran and K. Lehnert, Widely tunable parametric amplifier based on a superconducting quantum interference device array resonator, *Applied Physics Letters* **91**, 083509 (2007).
- [16] T. Yamamoto, K. Inomata, M. Watanabe, K. Matusuba, T. Miyazaki, W. D. Oliver, Y. Nakamura, and J. Tsai, Flux-driven Josephson parametric amplifier, *Applied Physics Letters* **93**, 042510 (2008).
- [17] T. Roy, S. Kundu, M. Chand, A. Vadiraj, A. Ranadive, N. Nehra, M. P. Patankar, J. Aumentado, A. Clerk, and R. Vijay, Broadband parametric amplification with impedance engineering: Beyond the gain-bandwidth product, *Applied Physics Letters* **107**, 262601 (2015).
- [18] D. Ezenkova, D. Moskalev, N. Smirnov, A. Ivanov, A. Matanin, V. Polozov, V. Echeistov, E. Malevannaya, A. Samoylov, E. Zikiy, *et al.*, Broadband SNAIL parametric amplifier with microstrip impedance transformer, *Applied Physics Letters* **121** (23), 232601 (2022).
- [19] R. Kaufman, T. White, M. I. Dykman, A. Iorio, G. Sterling, S. Hong, A. Opremcak, A. Bengtsson, L. Faoro, J. C. Bardín, *et al.*, Josephson parametric amplifier with Chebyshev gain profile and high saturation, *Physical Review Applied* **20**, 054058 (2023).
- [20] S. Boutin, D. M. Toyli, A. V. Venkatramani, A. W. Eddins, I. Siddiqi, and A. Blais, Effect of higher-order nonlinearities on amplification and squeezing in Josephson parametric amplifiers, *Physical Review Applied* **8**, 054030 (2017).
- [21] A. Remm, S. Krinner, N. Lacroix, C. Hellings, F. Swiadek, G. J. Norris, C. Eichler, and A. Wallraff, Intermodulation distortion in a Josephson traveling-wave parametric amplifier, *Physical Review Applied* **20**, 034027 (2023).
- [22] B. Ho Eom, P. K. Day, H. G. LeDuc, and J. Zmuidzinas, A wideband, low-noise superconducting amplifier with high dynamic range, *Nature Physics* **8**, 623 (2012).
- [23] M. Malnou, J. Aumentado, M. Vissers, J. Wheeler, J. Hubmayr, J. Ullom, and J. Gao, Performance of a kinetic inductance traveling-wave parametric amplifier at 4 Kelvin: Toward an alternative to semiconductor amplifiers, *Physical Review Applied* **17**, 044009 (2022).
- [24] S. Frasca, C. Roy, G. Beaulieu, and P. Scarlino, Three-wave-mixing quantum-limited kinetic inductance parametric amplifier operating at 6 T near 1 K, *Physical Review Applied* **21**, 024011 (2024).
- [25] J. Zmuidzinas, Superconducting microresonators:

- physics and applications, *Annu. Rev. Condens. Matter Phys.* **3**, 169 (2012).
- [26] C. Bockstiegel, J. Gao, M. Vissers, M. Sandberg, S. Chaudhuri, A. Sanders, L. Vale, K. Irwin, and D. Pappas, Development of a broadband NbTiN traveling wave parametric amplifier for MKID readout, *Journal of Low Temperature Physics* **176**, 476 (2014).
- [27] S. Shu, N. Klimovich, B. H. Eom, A. Beyer, R. B. Thakur, H. Leduc, and P. Day, Nonlinearity and wide-band parametric amplification in a (Nb, Ti) N microstrip transmission line, *Physical Review Research* **3**, 023184 (2021).
- [28] D. J. Parker, M. Savytskyi, W. Vine, A. Laucht, T. Duty, A. Morello, A. L. Grimsmo, and J. J. Pla, Degenerate parametric amplification via three-wave mixing using kinetic inductance, *Physical Review Applied* **17**, 034064 (2022).
- [29] M. R. Vissers, J. Hubmayr, M. Sandberg, S. Chaudhuri, C. Bockstiegel, and J. Gao, Frequency-tunable superconducting resonators via nonlinear kinetic inductance, *Applied Physics Letters* **107**, 062601 (2015).
- [30] K. Makise, H. Terai, M. Takeda, Y. Uzawa, and Z. Wang, Characterization of NbTiN thin films deposited on various substrates, *IEEE Transactions on Applied Superconductivity* **21**, 139 (2010).
- [31] D. Niepce, J. Burnett, and J. Bylander, High kinetic inductance NbN nanowire superinductors, *Physical Review Applied* **11**, 044014 (2019).
- [32] N. Samkharadze, A. Bruno, P. Scarlino, G. Zheng, D. DiVincenzo, L. DiCarlo, and L. Vandersypen, High-kinetic-inductance superconducting nanowire resonators for circuit QED in a magnetic field, *Physical Review Applied* **5**, 044004 (2016).
- [33] F. Faramarzi, R. Stephenson, S. Sypkens, B. H. Eom, H. LeDuc, and P. Day, A 4-8 GHz Kinetic Inductance Travelling-Wave Parametric Amplifier Using Four-Wave Mixing with Near Quantum-Limit Noise Performance, *arXiv preprint arXiv:2402.11751* (2024).
- [34] K. Peng, M. Naghiloo, J. Wang, G. D. Cunningham, Y. Ye, and K. P. O'Brien, Floquet-mode traveling-wave parametric amplifiers, *PRX Quantum* **3**, 020306 (2022).
- [35] J. Y. Mutus, T. C. White, R. Barends, Y. Chen, Z. Chen, B. Chiaro, A. Dunsworth, E. Jeffrey, J. Kelly, A. Megrant, *et al.*, Strong environmental coupling in a Josephson parametric amplifier, *Applied Physics Letters* **104**, 263513 (2014).
- [36] J. Grebel, A. Bienfait, É. Dumur, H.-S. Chang, M.-H. Chou, C. Conner, G. Peairs, R. Povey, Y. Zhong, and A. Cleland, Flux-pumped impedance-engineered broadband Josephson parametric amplifier, *Applied Physics Letters* **118**, 142601 (2021).
- [37] L. Ranzani, G. Ribeill, B. Hassick, and K. C. Fong, Wide-band Josephson parametric amplifier with integrated transmission line transformer, in *2022 IEEE International Conference on Quantum Computing and Engineering (QCE)* (IEEE, 2022) pp. 314–319.
- [38] O. Naaman and J. Aumentado, Synthesis of parametrically coupled networks, *PRX Quantum* **3**, 020201 (2022).
- [39] K. M. Sundqvist and P. Delsing, Negative-resistance models for parametrically flux-pumped superconducting quantum interference devices, *EPJ Quantum Technology* **1**, 1 (2014).
- [40] W. Getsinger, Prototypes for use in broadbanding reflection amplifiers, *IEEE Transactions on Microwave Theory and Techniques* **11**, 486 (1963).
- [41] N. Frattini, V. Sivak, A. Lingenfelter, S. Shankar, and M. Devoret, Optimizing the nonlinearity and dissipation of a snail parametric amplifier for dynamic range, *Physical Review Applied* **10**, 054020 (2018).
- [42] A. Zorin, Josephson traveling-wave parametric amplifier with three-wave mixing, *Physical Review Applied* **6**, 034006 (2016).
- [43] B. A. Mazin, *Microwave kinetic inductance detectors* (California Institute of Technology, 2005).
- [44] B. A. Mazin, Microwave kinetic inductance detectors: The first decade, in *AIP Conference Proceedings*, Vol. 1185 (American Institute of Physics, 2009) pp. 135–142.
- [45] J. R. Clem and V. Kogan, Kinetic impedance and depairing in thin and narrow superconducting films, *Physical Review B* **86**, 174521 (2012).
- [46] C. M. Caves, Quantum limits on noise in linear amplifiers, *Phys. Rev. D* **26**, 1817 (1982).
- [47] H. B. Callen and T. A. Welton, Irreversibility and generalized noise, *Physical Review* **83**, 34 (1951).
- [48] A. R. Kerr, M. J. Feldman, and S.-K. Pan, Receiver noise temperature, the quantum noise limit, and the role of the zero-point fluctuations, in *Proc. of the 8th Int. Symp. on Space Terahertz Technology* (1997) pp. 101–111.
- [49] M. Mirhosseini, E. Kim, X. Zhang, A. Sipahigil, P. B. Dieterle, A. J. Keller, A. Asenjo-Garcia, D. E. Chang, and O. Painter, Cavity quantum electrodynamics with atom-like mirrors, *Nature* **569**, 692 (2019).
- [50] J. Y. Qiu, A. Grimsmo, K. Peng, B. Kannan, B. Lienhard, Y. Sung, P. Krantz, V. Bolkhovskiy, G. Calusine, D. Kim, *et al.*, Broadband squeezed microwaves and amplification with a Josephson travelling-wave parametric amplifier, *Nature Physics* **19**, 706 (2023).
- [51] D. M. Pozar, *Microwave Engineering: Theory and Techniques* (John Wiley & Sons, 2021).
- [52] P. Kurpiers, T. Walter, P. Magnard, Y. Salathe, and A. Wallraff, Characterizing the attenuation of coaxial and rectangular microwave-frequency waveguides at cryogenic temperatures, *EPJ Quantum Technology* **4**, 1 (2017).
- [53] W. Dai, G. Liu, V. Joshi, A. Miano, V. Sivak, S. Shankar, and M. H. Devoret, Optimizing the pump coupling for a three-wave mixing Josephson parametric amplifier, *arXiv preprint arXiv:2411.07208* (2024).
- [54] G. Butseraen, A. Ranadive, N. Aparicio, K. Rafsanjani Amin, A. Juyal, M. Esposito, K. Watanabe, T. Taniguchi, N. Roch, F. Lefloch, *et al.*, A gate-tunable graphene Josephson parametric amplifier, *Nature Nanotechnology* **17**, 1153 (2022).
- [55] L. J. Splitthoff, J. J. Westorp, M. Pita-Vidal, A. Bargerboos, Y. Liu, and C. K. Andersen, Gate-tunable kinetic inductance parametric amplifier, *Physical Review Applied* **21**, 014052 (2024).
- [56] V. Sivak, S. Shankar, G. Liu, J. Aumentado, and M. Devoret, Josephson array-mode parametric amplifier, *Physical Review Applied* **13**, 024014 (2020).
- [57] D. P. Pappas, M. R. Vissers, D. S. Wisbey, J. S. Kline, and J. Gao, Two level system loss in superconducting microwave resonators, *IEEE Transactions on Applied Superconductivity* **21**, 871 (2011).
- [58] M. H. Devoret *et al.*, Quantum fluctuations in electrical circuits, *Proceedings of the Les Houches Summer School, Session LXIII*, edited by S. Reymaud, E. Gia-

- cobino, and J. Zinn-Justin (Elsevier Science, B.V., 1997) **7**, 133 (1995).
- [59] O. Astafiev, A. M. Zagoskin, A. Abdumalikov Jr, Y. A. Pashkin, T. Yamamoto, K. Inomata, Y. Nakamura, and J. S. Tsai, Resonance fluorescence of a single artificial atom, *Science* **327**, 840 (2010).